Supplemental Information

Copper coordination polymers with selective hole conductivity

Hannes Michaels[1,2], Matthias J. Golomb[3], Byeong Jo Kim[1], Tomas Edvinsson[4], Fabio Cucinotta[2], Paul G. Waddell[2], Michael R. Probert[2], Steven J. Konezny[5,6], Gerrit Boschloo[1], Aron Walsh[3,7] & Marina Freitag[2,1*]

[1] Department of Chemistry, Ångström Laboratory, Uppsala University, P.O. Box 523, SE-75120 Uppsala, Sweden
[2] School of Natural and Environmental Science, Bedson Building, Newcastle University, NE1 7RU Newcastle upon Tyne, UK
[3] Department of Materials, Imperial College London, Exhibition Road, London SW7 2AZ, UK
[4] Deptartment of Materials Science and Engineering, Solid-State Physics, Uppsala University, P.O. Box 35, SE-751 03, Uppsala, Sweden
[5] Energy Sciences Institute, Yale University, 520 West Campus Drive, West Haven, CT 06516, USA
[6] Department of Chemistry/Physics, Yale University, 225 Prospect Street, New Haven, CT 06511, USA
[7] Department of Materials Science and Engineering, Yonsei University, Seoul 03722, Korea
* marina.freitag@newcastle.ac.uk

Contents

Materials and Methods

Materials

Unless otherwise stated, all materials were used without further purification; synthesis grade solvents as well as microscope slides from VWR; Diisopropylamine, diphenylamine, copper(II) chloride as well as dry tetrahydrofurane, anisole, chlorobenzene, valeronitrile, cesium iodide, 4-*tert*-butyl pyridine (vacuum-distilled before use) and poly(3-hexyl thiophene) from Sigma-Aldrich; conductive glass substrates (TEC 15) from Pilkington; colloidal 15% SnO_2 precursor from Fisher Alfa Aesar; lead iodide/bromide perovskite precursors from TCI chemicals; organic salts for perovskite precursors such as formamidinium iodide from GreatCellEnergy (Dyesol/GreatCellSolar); dry dimethyl formamide and dimethyl sulfoxide from Acros Fisher Scientific; Spiro-MeOTAD (sublimed, 99.8%) and PEDOT:PSS from Borun Chemicals; Cobalt FK209 and the carbon paste from Dyenamo (Stockholm).

Methods

Instrumentation for characterization of compounds. ^{1}H and ^{13}C NMRs were recorded on a JEOL-400 MHz spectrometer. High-resolution mass spectroscopy was first internally performed in-house on a micrOTOF-Q II^{TM} ESI-Qq-TOF and later confirmed by Stenhagen Analyslab AB, Mölndal, Sweden. Elemental analysis was performed by Analytische Laboratorien Gmbh, Lindlar, Germany. Fourier-transformed infrared vibrational spectra were collected with a ThermoFischer Nicolet Avatar 370 DTGS and the vibrations assigned according to literature on dithiocarbamate compounds.[S1–S3]

Electrochemistry. Electrochemical characterization was carried out with an XR potentiostat (Ivium, Eindhoven, The Netherlands). Cyclic voltammetry was recorded using a three-electrode setup employing a 2 mm disk gold electrode and a porous graphite rod as working and counter electrode, respectively. Potentials were measured against a Ag/AgCl (0.1M $AgNO_3$) reference electrode. Voltammograms were recorded from 5 mM solutions at a scan speed of 20 mV/s in a 0.1 M 1:1 acetonitrile/chlorobenzene electrolyte of tetrabutylammonium hexaflourophosphate. The surface of the solutions was covered with N_2 gas flow. All potentials were subsequently calibrated against the ferrocene/ferrocenium redox couple. For Cu(II) complexes (compounds **6-7**), the scan was measured from positive potentials towards reduction. For the final Cu(II/I) polymers, the measurement commenced with the oxidative scan.

For the cyclic voltammetry, and other characterization of thin films, the copper coordination polymer films were deposited as described in the device fabrication, however, for amplification of sample volume, the spin-coating speeds were reduced to 1000 rpm and the concentrations raised to 25 mg/mL (see Fig. S19). The voltammograms of thin films were measured in an aqueous 0.1 M KCl electrolyte with a Pt wire as counter electrode, against a Ag/KCl (0.1 M) pseudo-reference electrode, which was subsequently calibrated versus $K_4Fe(CN)_6$. The standard redox potential of $K_4Fe(CN)_6$ of +0.370 V *vs* SHE allows conversion of the redox potential $\mathcal{E}$ to a value of energy E

versus vacuum level according to

$$E = q\mathcal{E}[\mathrm{V}\ vs\ \mathrm{SHE}] - 4.44\mathrm{eV} \tag{S1}$$

with the electron charge $q = -e$.

UV/Vis spectroscopy. Absorption spectra were measured using a HR-2000 spectrophotometer (Ocean Optics, Largo, FL, USA) with baseline correction from dichloromethane solutions of the complexes. The extinction coefficients ϵ were calculated from triple determination of concentrations and an ensuing linear regression.

X-ray diffraction. ***Single-crystal.*** Crystal structure data were collected at 100 K on beamline I19[S4, S5] at the Diamond Light Source using synchrotron radiation (λ = 0.68890 Å) and the data processed using the software APEX3. All structures were solved using XT[S6] and refined by XL[S7] using the Olex2 interface.[S8] All non-hydrogen atoms were refined anisotropically and hydrogen atoms were positioned with idealised geometry. The displacement parameters of the hydrogen atoms were constrained using a riding model with U_{H} set to be an appropriate multiple of the U_{eq} value of the parent atom. ***Powder.*** Powder X-ray diffraction measurements were performed on a PANalytical X´Pert Pro-MPD powder diffractometer in the 2θ range 5–60°, a step size of 0.0334° with 1 s step^{-1} intervals. ***Thin film.*** Grazing incidence X-ray diffractograms of films were recorded using a Siemens D5000 q–2q diffractometer and employing a parallel-plate Soller-slit collimator (0.3x resolution) with Cu Kα1 (λ = 1.54056 Å) radiation hitting the sample at a grazing incidence angle (θ) of 3°. The instrument was set to the detector scan mode, using the Diffrac plus XRD Commander program, and the diffraction pattern was measured over the Bragg angle (2θ) range of 5° to 60°.

Raman spectroscopy. Raman spectra were collected using an InVia spectrometer (Renishaw, New Mills, UK) in confocal mode with a 50x objective, a frequency doubled Nd:YAG laser operating at 532 nm, and a Rayleigh line filter cutting 80 cm^{-1} into the Stokes part of the spectra. A 2400 lines/mm grating was used and the 520.5 cm^{-1}line of Si was used as a calibration giving a resolution of 1 cm^{-1} The Raman spectra were recorded at different spots and laser intensities to confirm the homogeneity of the material. The measurements were either taken from a powder sample or from a film spin-coated onto FTO as indicated. In the latter case, purposely thicker films were deposited by limiting the spin-coating speed to 1000 rpm, similar to thin-film XRD (see Fig. S19).

Scanning Electron Microscopy. Scanning electron microscopy was performed using a Zeiss LEO1550 microscope. Magnification parameters are annotated in each picture.

Hole mobility. FTO glass substrates were patterned, washed, and ozone-treated as described above. A hole-injecting layer of poly(3,4-ethylenedioxythiophene)-poly(styrenesulfonate) (PEDOT:PSS)

was deposited from an aqueous, with two parts isopropanol diluted solution (9 s@1000 rpm; 30 s@2000 rpm) and annealed at 150 °C for 20 minutes. The hole transport material solutions were mixed and deposited as described in the solar cell fabrication section. In the case of Spiro-MeOTAD, difficulties wetting the surface required pre-heating the substrate to around 70 °C, which resulted in a somewhat thicker layer (Fig. S25). The hole transport material solutions were mixed and deposited as described in the solar cell fabrication section. Finally, a gold electrode was thermally evaporated onto the samples as described in the solar cell fabrication. The J-V scans were recorded in a voltage range from 0 to 6 V using a Keithley 2400 digital source meter. The samples were covered with a black blanket to exclude photoinduced effects. Crosssectional electron microscope images were taken of each sample to determine the thickness of the test layer. The hole mobility μ was then calculated using Mott-Gurneys law,

$$J(V) = \frac{9}{8}\epsilon\epsilon_0\mu\frac{V^2}{d^3} \tag{S2}$$

where J is the current density, V the potential, ϵ_0 the vacuum permittivity and d the layer thickness, while assuming a value of 3 for the relative permittivity ϵ for non-metallic semiconductors after Snaith and Grätzel.[S9]

Temperature-dependent conductivity. For the temperature-dependent conductivity, interdigitated gold electrodes were deposited onto non-conductive circular sapphire glass substrates (Glanzmann, 10 mm diameter) via photolithography. The pattern of 300 10 μm wide fingers between the 8 mm apart contacts created a channel of 50 μm width and 0.88 m length. After plasma cleaning of the substrates, positive AZ1505 photoresist was spin-coated (8 s@300 rpm, 50 rpm/s; 45 s@3000 rpm, 200 rpm/s) and dried 50 seconds at 100 °C. Subsequently, the substrates were mounted into a Suss Microtec MJB4 mask aligner and illuminated 7 seconds with 365 nm light. Immediately after, the films were immersed in AZ400K developer for 25 seconds, rinsed with deionized water and dried under dry air flow. Ensuing, 10 nm chromium followed by 150 nm gold were deposited onto the samples by thermal evaporation. Subsequently, the photoresist was lifted off using ultrasonication in an acetone bath. The fingers were then examined through an Olympus optical microscope (example see Fig. S26). The hole transport material films to examine were then dropcasted from valeronitrile solutions (additives and concentrations as in the solar cells) and left to dry in ambient atmosphere.

For the temperature-dependent measurement, the samples were loaded into a Janis CCS-100/204N cryostat, equipped with a Zephyr HC-4A cooling unit and a LakeShore 335 temperature control. The conductivity was measured using an Agilent B1500A semiconductor device analyzer. Equipped with with medium-power source-measurement modules as well as atto-sense and switch units for high-resolution current sensing, I–V data were then obtained from 10 to 310 K. The conductivity was obtained by fitting the measured resistance data to a computational model using the ac/dc module in the COMSOL Multiphysics software. After the measurements, the thickness of the films was examined at multiple locations with a ZYGO Ametek optical profilometer.

The temperature-dependent conductivity σ was fitted with a first order Arrhenius model as

$$\sigma = A\exp(\frac{E_A}{k_BT}) \tag{S3}$$

with A as the prexponential factor, E_A the thermal activation energy, k_B Boltzmann's constant and T the temperature.

Density functional theory calculations. All calculations were performed with the all-electron electronic structure code FHI-Aims[S10–S14]. Geometry relaxations were initialized with the *light* basis set and the PBEsol functional, followed by a relaxation with the HSE06 functional and the *light* basis set, and finished with a relaxation with HSE06 and the *intermediate* basis set. Convergence parameters were left at their code default values. All electronic structure calculations were carried out with the *tight* basis set and the HSE06 functional on a $4 \times 4 \times 4$ k-point grid. Polaron calculations were done using the occupation matrix formalism in the DFT+U framework, with the PBE functional and on a $2 \times 2 \times 1$ k-point grid. Additional details can be found in the SI and the dedicated repository.

Photoluminescence. Steady-state photoluminescence spectra were recorded on a Varian Eclipse Fluorescence spectrometer. The excitation wavelength was 450 nm. The samples were illuminated from the glass side. For every sample, the emission spectrum of the not-quenched perovskite was recorded prior to the deposition of the HTM layer to allow for normalization of sample-to-sample fluctuations. To determine potential photoluminescence quenching by ambient oxygen or the like on the perovskite surface, the emission intensity was checked after sealing the perovskite with a thin layer of poly(methyl methacrylate), which did not lead to an increase in emission intensity larger than the sample-to-sample variation. The relative quenched intensity for each hole conductor was scaled to its not-quenched perovskite to compare the extraction efficiencies.
Photoluminescence lifetimes were recorded at the emission center of 780 nm on an Edinburgh FLS980 spectrometer. Samples were excited with an EPL-475 (472 nm, 61 ps pulse width) picosecond laser, and measured with a time-correlated single photon counting module and a Hamamatsu R928P photomultiplier tube (in fan assisted TE cooled housing, operating temperature -20 °C). Lifetime fits of the photoluminescence intensity I were extracted directly in the F980 software with numerical data reconvolution based on Marquardt-Levenberg algorithm, with exponential traces as

$$I = \sum_i B_i e^{\frac{1}{\tau}t}, \tag{S4}$$

with amplitude factors B_i and time constants τ_i. To present the traces, the counts of photons before time-zero were averaged to serve as a baseline. Then, the relative amplitudes in all scans were rescaled between the common baseline and the peak intensity normalized to 1.

Characterization of solar cells. Current–voltage measurements were carried out in ambient air under AM 1.5G illumination using a self-calibrating Sinus-70 solar simulator (Wavelabs, Leipzig, Germany). An X200 source meter (Ossila, Sheffield, UK) was used to assess solar cell performance (scan speed 100 mV s^{-1}). A mask was employed to confine the active solar cell area to 0.125 cm^2. In general, for Au-contacted cells, at least four solar cells (carrying four pixels each) were fabricated for each sample type to obtain 16 measurements; in case of carbon counter elec-

trodes (with two contacts per substrate) at least six substrates of the same type were manufactured to obtain 12 measurements. A balance-adjusted hysteresis index HI as proposed by Nemnes et al. was calculated as

$$HI = \frac{\eta_{\mathrm{rev}} - \eta_{\mathrm{forw}}}{\eta_{\mathrm{rev}} + \eta_{\mathrm{forw}}}, \tag{S5}$$

with $\eta_{\mathrm{forw,rev}}$ as the conversion efficiencies from forward and reverse scans, respectively.[S15] Outliers of large error ($>25\%$) were excluded from statistical analysis. The stabilized power output was recorded under maximum-power-point-tracking. To evaulate the susceptibility of the different device types to air and moisture, the samples were kept in ambient atmosphere (in dark), and the J-V responses were measured in recurring intervals.

Incident-photon-to-current conversion efficiency. IPCE spectra were recorded with an ASB-XE-175 xenon light source (10 mW cm^{-2}) (Spectral Products, Putnam, CT, USA) and a CM110 monochromator (Spectral Products, Putnam, CT, USA). The photocurrent was measured with a U6 digital acquisition board (LabJack, Lakewood, CO, USA). The setup was calibrated with a certified silicon reference cell (Fraunhofer ISE, Munich, Germany). Photocurrents were integrated based on the spectral distribution of sunlight (AM 1.5G).[S16]

Synthesis

In general, the preparation of coordination polymers followed the scheme in Fig. S1 and each step is described in detail on the ensuing pages.
Authors' notes concerning the preparation of compounds **1**-**7**:

1. Okubo et al. described the polymerization of similar copper coordination polymers to occur quite rapidly (i.e. five minutes of stirring at room temperature). With our newly introduced ligands, the degree of polymerization after this time was very low. This was concluded from, e.g. in the case of preparing polymer **2**, the entire copper(I) halide still floating in the reaction mixture.

2. The authors attempted to synthesize the missing coordination polymer by reacting copper(II) (diphenyl dithiocarbamate) (compound **5**) with copper(I) iodide. However, due to the high reduction potential of copper(II) (diphenyl dithiocarbamate) (compound **5**) of 0.67 V vs NHE, the addition of copper(I) iodide, instead of forming a coordination polymer, rather gave the oxidation of the $3\ I^- \rightarrow I_3^- + 2\ e^-$ redox couple (0.35 V vs NHE) and hence the reduction of and decomplexation of the copper(II) (diphenyl dithiocarbamate), which was observed by green precipitate.

3. The filtration step after all three polymerization reactions (**1**-**3**), but especially those with $CuBr{\cdot}S(CH_3)_2$, often isolated ample amounts of insoluble black solids. It is likely that these compounds consisted of similarly constructed macromolecules, however with such a high degree of polymerization that rendered their solubility poor. The solution processability of the presented compounds is a crucial property towards the device fabrication, hence, the here described purification methods were applied to isolate the allegedly shorter but processable polymer chains. The relation of synthetic conditions and the exact molecular properties of these copper coordination polymers, such as the degree of polymerization, are not part of the scope of this study, however, deserve more thorough investigation.

4. *N*-butyl lithium was chosen for the deprotonation of diphenylamine (reaction **5**) after several attempts with various hydroxide bases (LiOH/NaOH/KOH), despite being described in literature, proved unsuccessful.

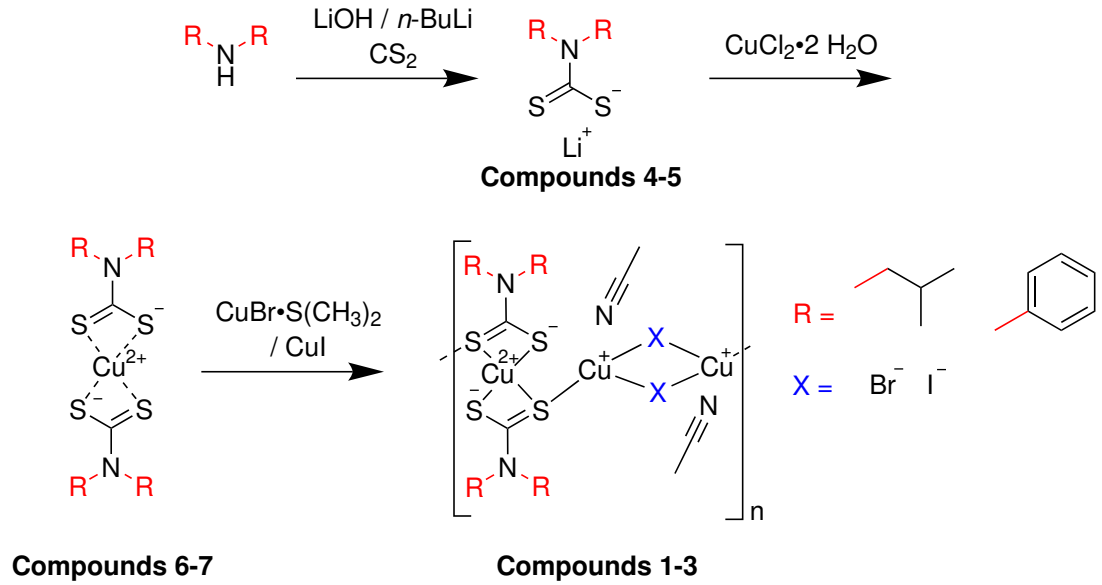

Figure S1: Overview scheme of the synthetic pathways used to prepare compounds **1**-**7**.

Preparation of $[Cu^{I}_{2}Cu^{II}Br_2((C_4H_9)_2NCS_2)_2(CH_3CN)_m]_n$ (compound **1**)

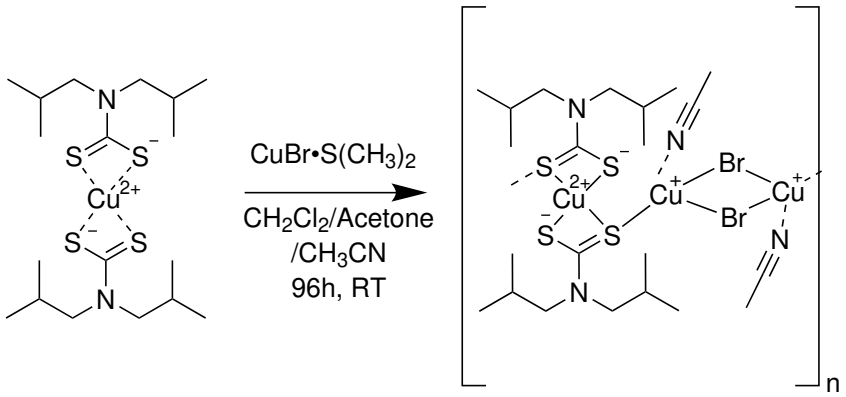

Compound 6 **Compound 1**

Figure S2: Preparation of compound **1**.

The general procedure for preparation of compound **1** was modified from Okubo et al.'s method.[S17] 0.500 g (1.06 mmol, 1 eq) of copper (diisobutyl dithiocarbamate) (compound **6**) were dissolved in a mixture of dichloromethane, acetone and acetonitrile (10 mL each). After the addition of 0.435 g (2.12 mmol, 2 eq) copper(I) bromide dimethyl sulfide, the reaction mixture was stirred at room temperature for four days, and subsequently dried of solvents using rotary evaporation. The obtained crude product was dissolved in dichloromethane, the solution filtered) and left to evaporate in ambient atmosphere to obtain black solids within several days (69%).

FT-IR (cm^{-1}): C-H stretch 2958, 2928, 2869; acetonitrile CH_3 stretch 2923; acetonitrile C≡N stretch 2222; (CS_2)-N stretch 1520, 1336; CH_3 bend (methylene group) 1464; geminal dimethyl CH_3 bend 1387; (CH_2)-N stretch 1253, 1151; C=S stretch 1186; (CS_2) asymmetric stretch 955; multisubstituted C-H bend 922, 878, 820. Elemental analysis (calculated/found (%)): C 33.88/31.82; H 5.80/5.15; Cu 20.31/21.51; N 5.37/6.32; S 18.45/14.47.

Preparation of $[Cu^{I}_{2}Cu^{II}Br_2((C_4H_9)_2NCS_2)_2(CH_3CN)_m]_n$ (compound **2**)

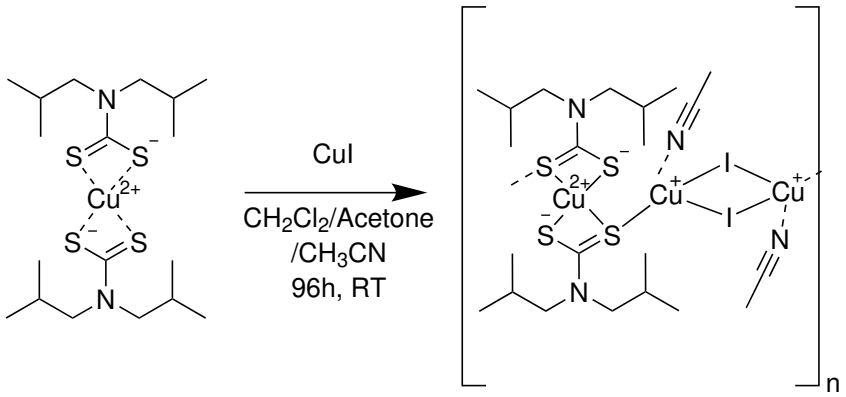

Compound 6 **Compound 2**

Figure S3: Preparation of compound **2**.

The general procedure for preparation of compound **2** was modified from Okubo et al.'s method.[S17] 0.500 g (1.06 mmol, 1 eq) of copper (diisobutyl dithiocarbamate) (compound **6**) were dissolved in a mixture of dichloromethane, acetone and acetonitrile (10 mL each). After the addition of 0.403 g (2.12 mmol, 2 eq) copper(I) iodide, the reaction mixture was stirred at room temperature for four days, and subsequently dried of solvents using rotary evaporation. The obtained crude product was dissolved in dichloromethane, the solution filtered and left to evaporate in ambient atmosphere to obtain black solids within several days (73%).

FT-IR (cm^{-1}): C-H stretch 2959, 2927, 2869; acetonitrile CH_2 stretch 2924; acetonitrile C≡N stretch 2225; (CS_2)-N stretch 1496, 1336; CH_3 bend (methylene group) 1464; geminal dimethyl CH_3 bend 1387; (CH_2)-N stretch 1252, 1149; C=S stretch 1187; (CS_2) asymmetric stretch 958; multisubstituted C-H bend 920, 878, 823. Elemental analysis (calculated/found (%)): C 30.63/31.75; H 5.24/5.15; Cu 19.44/18.02; N 5.71/4.22; S 13.08/14.17.

Preparation of $[Cu^{I}_{2}Cu^{II}Br_2((C_6H_5)_2NCS_2)_2(CH_3CN)_m]_n$ (compound **3**)

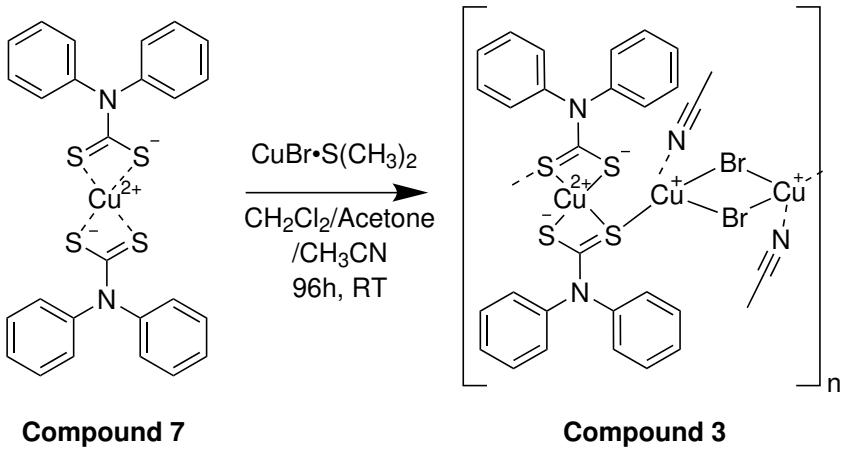

Compound 7 **Compound 3**

Figure S4: Preparation of compound **3**.

The general procedure for preparation of compound **3** was modified from Okubo et al.'s method.[S17] 0.773 g (1.4 mmol, 1 eq) of copper (diphenyl dithiocarbamate) (compound **7**) were dissolved in a mixture of dichloromethane, acetone and acetonitrile (10 mL each). After the addition of 0.575 g (2.8 mmol, 2 eq) copper(I) bromide dimethyl sulfide, the reaction mixture was stirred at room temperature for four days, and subsequently dried of solvents using rotary evaporation. The obtained crude product was dissolved in dichloromethane, the solution filtered and left to evaporate in ambient atmosphere to obtain black solids within several days (52%).

FT-IR (cm^{-1}): acetonitrile CH_3 stretch 2920, 2848; acetonitrile C≡N stretch 2245; aromatic C-H stretch 1590; (CS_2)-N stretch 1488, 1261; $(C_6H_5)_2$-N aromatic amine stretch 1387, 1372; C=S stretch 1046; (CS_2) asymmetric stretch 1001; aromatic C=C stretch 913, 878, 830; aromatic C-H bend 751, 747, 692, 686. Elemental analysis (calculated/found (%)): C 41.02/44.87; H 3.65/3.16; Cu 19.73/11.98; N 5.80/4.38; S 13.27/18.77.

Preparation of *Lithium (diisobutyl dithiocarbamate) trihydrate* (compound **4**))

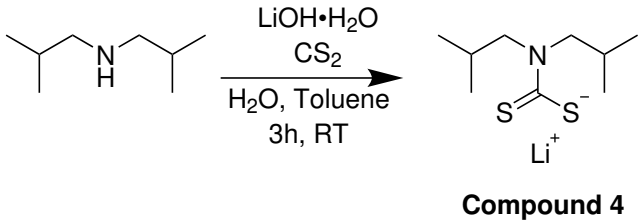

Figure S5: Preparation of compound **4**.

In general, the synthesis of compound **4** was adapted from the protocol Ngo et al. proposed.[S18] 2 mg (48 mmol, 1.2 eq) lithium hydroxide monohydrate were dissolved in 3 mL water. 2.84 mL (3.60 g, 48 mmol, 1.2 eq) of carbon disulfide were mixed into 25 mL toluene and added into the reaction mixture. To the resulting slurry, 6.99 mL (5.16 g, 40 mmol, 1 eq) of diisobutylamine was dropwise added. After a few minutes, the reaction mixture took on a pale yellow color under mild heat generation. The reaction was stirred for three hours at room temperature. Thereafter, the mixture was dried of solvents via rotary evaporation. The crude product was dissolved in diethyl ether and the mixture was filtered to remove excess hydroxide. After the volume of the diethyl ether phase was reduced to 5-10 mL through rotary evaporation, petroleum ether was poured into the flask and caused precipitation of white to pale yellow solids. The solids were washed with petroleum ether under ultrasonication, obtained via filtration and subsequently dried under high vacuum for 48 hours (98%).

^{1}H NMR (400 MHz, Acetonitrile-d3) δ 3.38 (d, J = 7.4 Hz, 4H), 2.06 (s, 6H), 1.52 – 1.42 (m, 2H), 0.41 (d, J = 6.7 Hz, 12H). ^{13}C NMR (101 MHz, Acetonitrile-d3) δ 212.87, 60.83, 26.83, 19.61. ESI *m/z* M^- calculated -204.0886, found -204.0739. FT-IR (cm^{-1}): O-H stretch (hydrate) 3500-3050; (CS_2)-N stretch 1473, 1289; CH_3 bend (methylene group) 1458; O-H bend (hydrate) 1402; geminal dimethyl CH_3 bend 1384; (CH_2)-N stretch 1232, 1147; C=S stretch 1198; (CS_2) asymmetric stretch 972; multisubstituted C-H bend 937, 909, 868, 820, 806.

Preparation of *Lithium (diphenyl dithiocarbamate)* (compound **5**))

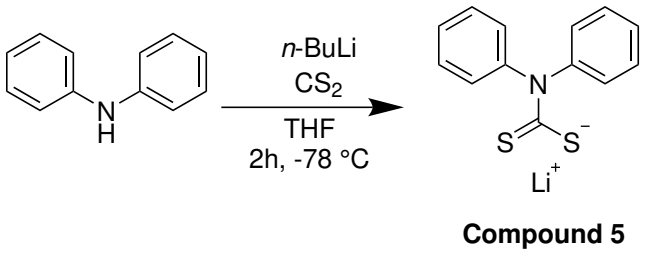

Figure S6: Preparation of compound **5**.

Compound **5** was synthesized in a slightly altered protocol adapted from Padungros et al.'s scheme.[S19] 4.56 mL (27 mmol, 1 eq) diphenylamine were mixed into 30 mL anhydrous tetrahydrofuran under inert gas on an acetone/dry ice bath (-78 °C). The temperature of the reaction mixture was let to equilibrate. Thereafter, 11.2 mL (1.86 g, 29 mmol, 1.07 eq) of a 2.6 M hexane solution of n-butyllithium were dropwise added into the reaction mixture over a period of 30 minutes. The mixture was stirred for another 30 minutes before the equally careful addition of 2.9 mL (3.64 g, 48 mmol, 1.78 eq) carbon disulfide. An immediate deep red color was observed and after 30 minutes, the reaction was removed from the dry ice bath. When reaching room temperature, petroleum ether was poured into the reaction, causing a colorless to light brown solid to precipitate. The solids where washed with petroleum as well as diethyl ether under ultrasonication, obtained via filtration and dried under high vacuum for 48 hours (98%).

^{1}H NMR (400 MHz, Acetonitrile-d3) δ 7.43 – 7.25 (m, 8H), 7.21 – 7.12 (m, 2H). ^{13}C NMR (101 MHz, Deuterium Oxide) δ 216.15, 148.66, 130.02, 127.89, 127.73. ESI *m/z* M^- calculated -244.0260, found -243.9865. FT-IR (cm^{-1}): aromatic C-H stretch 1626, 1593, 1585; (CS_2)-N stretch 1489, 1270; ($C_6H_5)_2$-N aromatic amine stretch 1330; C=S stretch 1047; (CS_2) asymmetric stretch 1002; aromatic C=C stretch 911, 883, 821; aromatic C-H bend 758, 750, 702, 691.

Preparation of *Copper (diisobutyl dithiocarbamate)* (compound **6**))

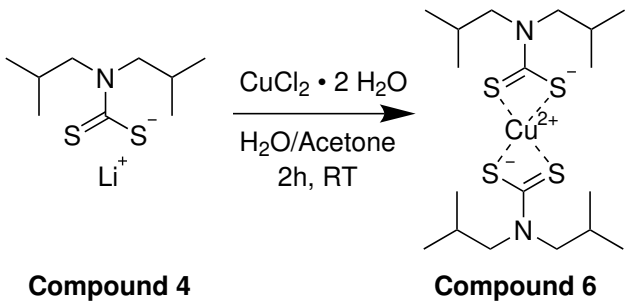

Figure S7: Preparation of compound **6**.

The general procedure for preparation of compound **6** was adapted from Ngo et al.'s report.[S18] 0.546 g (3.2 mmol, 1 eq) of copper(II) chloride dihydrate were dissolved in a mixture of 50 mL water and 20 mL acetone at room temperature. 1.70 g (6.4 mmol, 2 eq) of lithium (diisobutyl dithiocarbamate) trihydrate (compound **4**) were added, leading to the formation of a brown precipitate. After two hours, the reaction mixture was filtered. The obtained dark crude product was redissolved diethyl ether and dried with sodium sulfate. The diethyl ether was removed under rotary evaporation and the product finally dried under high vacuum for 24 hours (97%).

ESI *m/z* $M+H^+$ calculated 472.1130, found 472.1100. FT-IR (cm^{-1}): C-H stretch 2958, 2924, 2870; (CS_2)-N stretch 1500, 1288; CH_3 bend (methylene group) 1462; geminal dimethyl CH_3 bend 1385; (CH_2)-N stretch 1254, 1153; C=S stretch 1196; (CS_2) asymmetric stretch 984; multisubstituted C-H bend 918, 868, 818; Cu-$(CS_2)_2$ 428.

Preparation of *Copper (diphenyl dithiocarbamate)* (compound **7**))

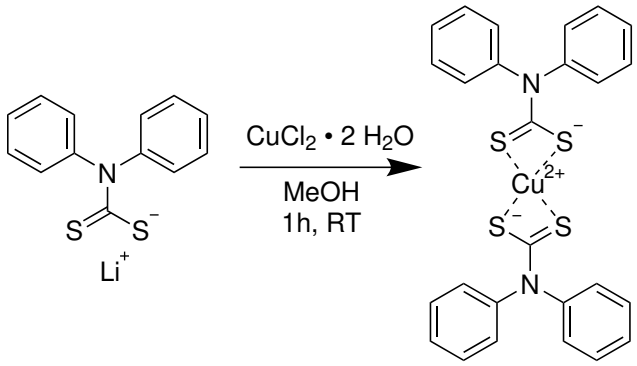

Figure S8: Preparation of compound **7**.

The general procedure for preparation of compound **7** was modified from Ngo et al.'s report.[S18] 2.01 g (8 mmol, 2 eq) of lithium (diphenyl dithiocarbamate) (compound **5**) were dissolved in 30 mL methanol. Upon addition of 0.681 g (4 mmol, 1 eq) copper(II) chloride dihydrate, black solids immediately precipitated. The mixture was let to stir for one hour at room temperature, after which the solids were obtained via filtration. The crude product was washed with more methanol under ultrasonication before being isolated through filtration. Finally, the solids were dried under high vacuum for 24 hours (94%).

ESI *m/z* M^+ calculated 550.9805, found 550.9676. FT-IR (cm^{-1}): aromatic C-H stretch 1588; (CS_2)-N stretch 1489, 1269; ($C_6H_5)_2$-N aromatic amine stretch 1392, 1368; C=S stretch 1050; (CS_2) asymmetric stretch 1002; aromatic C=C stretch 911, 881, 831; aromatic C-H bend 756, 749, 694, 686.

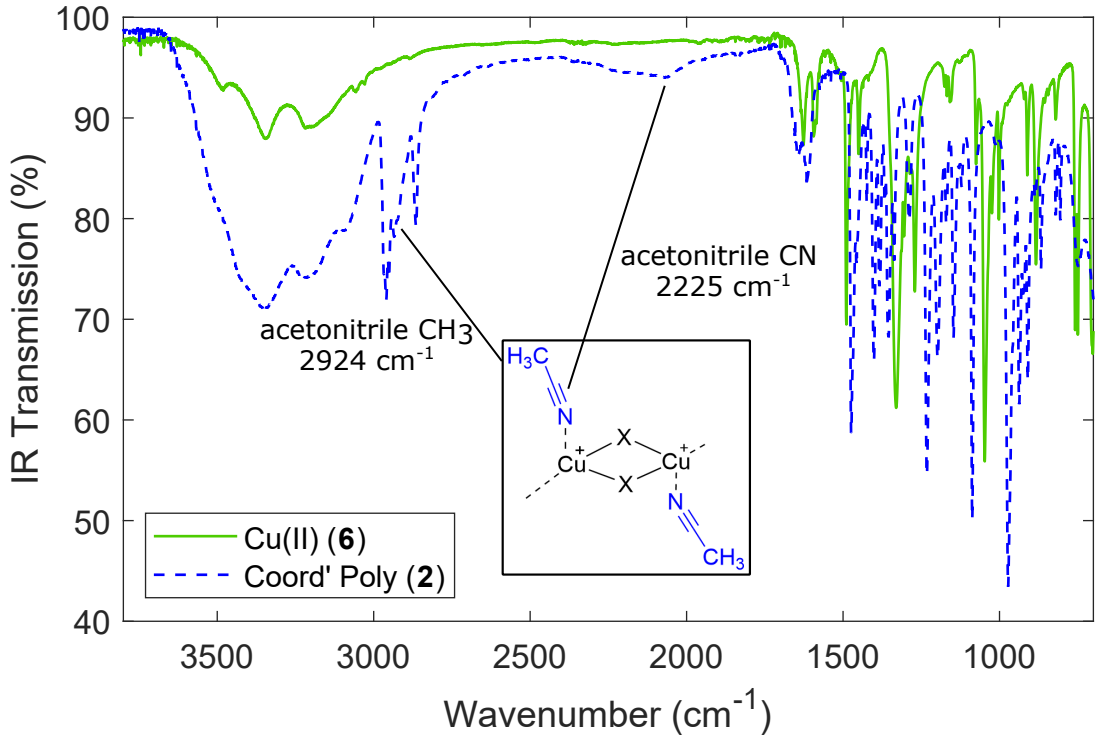

Figure S9: IR spectra comparing Cu(II) building block **6** to coordination polymer **2**. The insertion of Cu(I) halide units becomes apparent from the acetonitrile C≡N vibration at 2225 cm^{-1}.

Fabrication of solar cells

The n-i-p perovskite solar cells were assembled following a low-temperature approach. The perovskite layer was deposited with what is in literature known as a *two-step* method, to give samples of FTO/SnO_2/PVSK/HTM/[Au/C]. In detail, the conductive F:SnO_2 TCO electrodes were patterned with Zn/HCl and then washed in an RBS detergent solution, subsequently in acetone, ethanol and finally deionized water. After drying under N_2 flow, the glasses underwent 30 minutes of UV/ozone treatment. The glasses were broken into twin-substrates with the dimensions of 2.9x2.4 cm, which would eventually be split into two separate substrates with four electronic contact pads per sample. Prior to the following deposition of the SnO_2 *n*-selective layer, an interlayer of poly(allylamine hydrochloride) was deposited to improve the homogeneity of the subsequent SnO_2 layer, as demonstrated by Kim[S20] and Han[S21]. The ozone-treated substrates were mounted onto the spin-coater, and the surface covered with an appropriate amount of 1 mg/mL aqueous PAH solution, which had been ultrasonicated and then filtered.. The solution was let rest for one minute, before spinning for 30 seconds@3000 rpm (3000 rpm/s). Then, 1 mL deionized water was poured onto the substrate, followed by another spinning step of 20 seconds@5000 rpm (5000 rpm/s). For the tin oxide precursor, the commercial colloidal SnO_2 solution was diluted with four parts of a filtered, aqueous 1.5 mg/mL solution of potassium fluoride. 300 µL of the SnO_2 solution were then spread onto the sample, spun 30 seconds@3000 rpm (3000 rpm/s), and annealed 150 °C for 30 minutes in ambient air. Subsequently, a second UV/Ozone step of 25 minutes ensued, after which the substrates were transferred into a N_2 glovebox.

For the two-step deposition of the photoactive perovskite layer, the precursors were prepared, in an Ar glovebox, as follows: 1.3 M (630 mg) of PbI_2 per 0.9 mL dimethyl formamide and 0.1 mL dimethyl sulfoxide, with the additive of 1.9 mg/mL cesium acetate. This precursor was generally prepared a day in advance to the sample deposition, let dissolve over night on a 70 °C hotplate, filtered prior to deposition and kept at 70 °C throughout the deposition. The second solution contained 0.11 M (80 mg) methylammonium chloride (MACl), 0.04 M (64 mg) methylammonium iodide (MAI) and 0.47 M formamidinium iodide (FAI) in 10 mL isopropanol, which was prepared just before sample deposition.

50µL Cs:PbI_2 solution was carefully spread onto the ozone-treated substrates and spun 20 seconds@1500 rpm (5000 rpm/s), 30 seconds@5000 rpm (5000 rpm/s). The substrates were dried at 70 °C for one minute and then let cool to room temperature. Mounted back on the spin-coater, 350 µL of the [FA,MA][Cl,I] solution was poured onto the sample and spun for 30 seconds@2000 rpm (5000 rpm/s). Then, the substrates were quickly transferred out of the N_2 glovebox and annealed in ambient air at 140 °C for 25 minutes to give a $[Cs_{0.01}FA_{0.91}MA_{0.08}]PbI_3 \cdot 0.45$ MACl perovskite. Subsequently, the samples were moved back into the N_2 glovebox for deposition of the *p*-selective layers (hole transport materials, HTMs).

The solutions of the copper coordination polymer hole transport materials were prepared at 5 mg/mL (around 5 mM of repeating units) in chlorobenzene, containing 5 µL (per mL, 33 mM) 4-*tert*-butyl pyridine as an additive. In case of the less-soluble phenyl-ligand polymer **3**, half a volume equivalent of chloroform was added and the solution filtered after ultrasonication prior to the deposition. 40 µL of the solutions were dynamically coated onto the perovskite layer for 30 seconds@5000 rpm

(5000 rpm/s), after which the layer was quickly dried at 70 °C for two minutes. The cooled-down copper coordination polymer layers were sealed with a thin film of reduced graphene oxide (rGO) as proposed by Grätzel's group[S22] for their CuSCN HTM layer, by dynamically spin-coating an ultrasonically dispersed 1 mg/mL chlorobenzene solution of rGO for 30 seconds@3000 rpm (3000 rpm/s).

For reference cells, a 70 mM solution of Spiro-MeOTAD was prepared by mixing 42.9 mg Spiro-MeOTAD in 468 µL chlorobenzene, with additives of 230 mM 4-*tert*-butyl pyridine (16.9 µL), 35 mM lithium bis(trifluoromethane)sulfonimide (LiTFSI) and 2.1 mM tris(2-(1H-pyrazol-1-yl)-4-tert-butylpyridine)cobalt(III) tri[bis(trifluoromethane)sulfonimide] (FK209). The latter two were added from acetonitrile stock solutions, 9.6 µL of a 520 mg/mL LiTFSI solution and 5.3 µL of 300 mM cobalt FK209. 40 µL of the Spiro-MeOTAD precursor was dynamically coated onto the perovskite layer for 25 seconds@4000 rpm (4000 rpm/s). For further reference cells, poly(3-hexyl thiophene) (P3HT) was dissolved at 10 mg/mL in chlorobenzene with no further additives and 40 µL deposited dynamically at 3000 rpm for 30 seconds (3000 rpm/s).

For gold counter electrodes, the samples were placed in a LEICA EM MED020 metal evaporator. A strong current of around 60 A was directed through a tungsten boat carrying a small Au sphere underneath the samples. The film deposition was monitored with a LEICA EM QSG100 quartz crystal. Alternatively, for carbon counter electrodes, the samples were masked appropriately with commercial kapton tape, and a carbon paste was applied through doctor-blading, ensued by drying at 100 °C for 20 minutes on a hotplate.

For photoluminescence measurements, a 'one-step' perovskite layer was used which we found to form more uniform films on bare microscope slides. The stochiometric composition of the perovskite was adapted to resemble the electronic properties of the two-step perovskite used for solar cell devices, which was confirmed by a similar emission wavelength. As such, 20.7 mg (0.079 M) cesium iodide, 233.9 mg (1.36 M) formamidinium iodide, 17.9 mg (0.159 M) methylammonium bromide, 30.2 mg (0.45 M) methylammonium chloride, 663.9 mg (1.44 M) lead(II) iodide and 58.7 mg (0.159 M) lead(II) bromide were mixed in 700 µL dimethyl formamide and 300 µL dimethyl sulfoxide and left to dissolve over night on a 70 °C hotplate. Microscope glass slides (non-conductive) were washed and ozone-treated as described above. In a N_2 glovebox, the filtered and 70 °C warm precursor was spread onto the substrates, spun at 5000 rpm for 25 seconds, during which, after 15 seconds, 250 µL dry anisole was poured onto the sample.[S23] The perovskites were annealed for 20 minutes at 130 °C (in N_2). The HTM layers were then deposited as described above, the sealing rGO layer was omitted for this measurement.

Electrochemistry

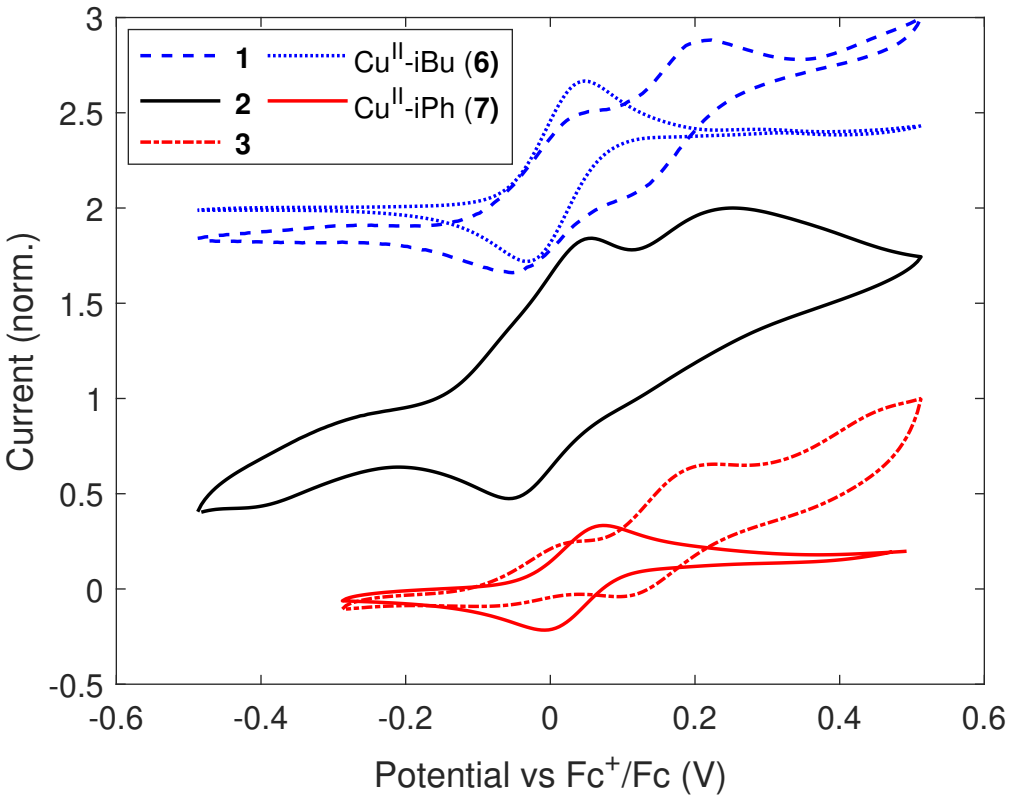

Figure S10: Cyclic voltammograms of coordination polymers **1**-**3**, overlayed with scans of the corresponding Cu(II) units **6**-**7**.

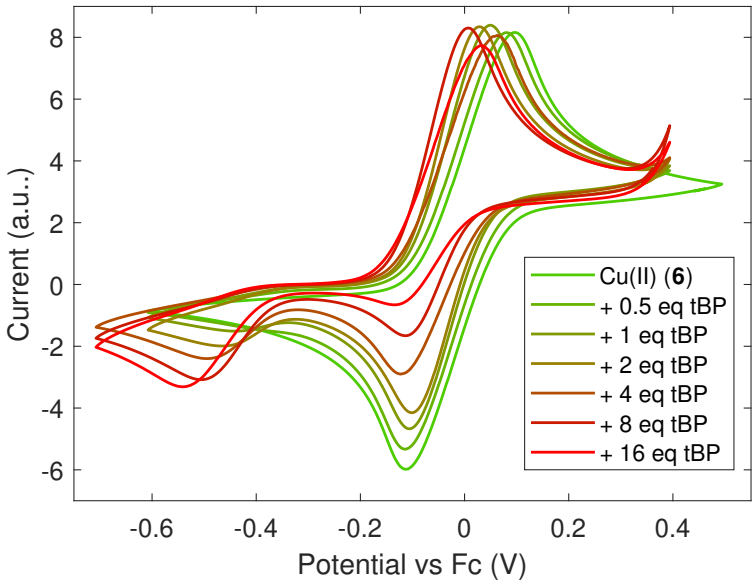

Figure S11: Cyclic voltammograms of Cu(II) unit **6** under the addition of 4-*tert*-butyl pyridine.

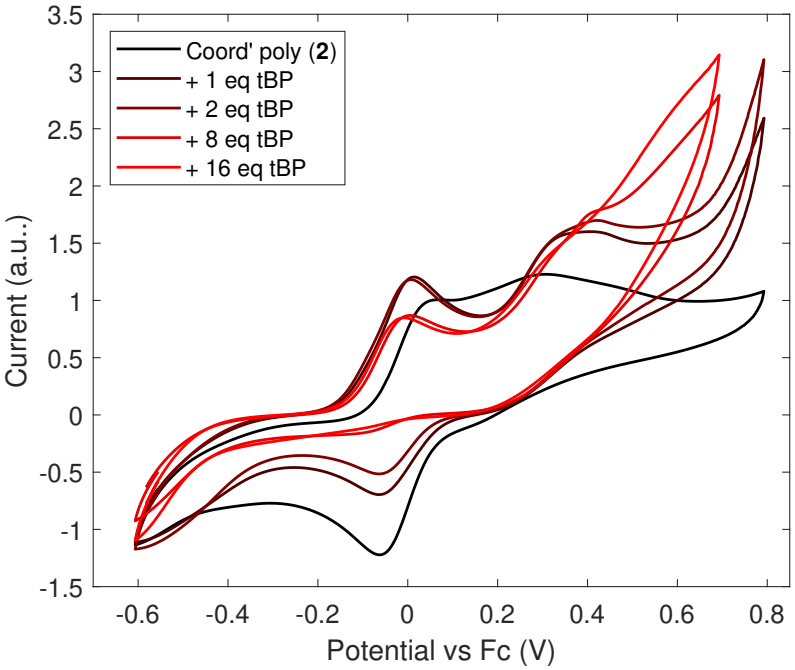

Figure S12: Cyclic voltammograms of copper coordination polymer **2** under the addition of 4-*tert*-butyl pyridine. The equivalents are in ratio to the Cu(II) units. For clarity some measurements were omitted from the graph. The precursors for depositing thin films contained around 3-4 eq tBP.

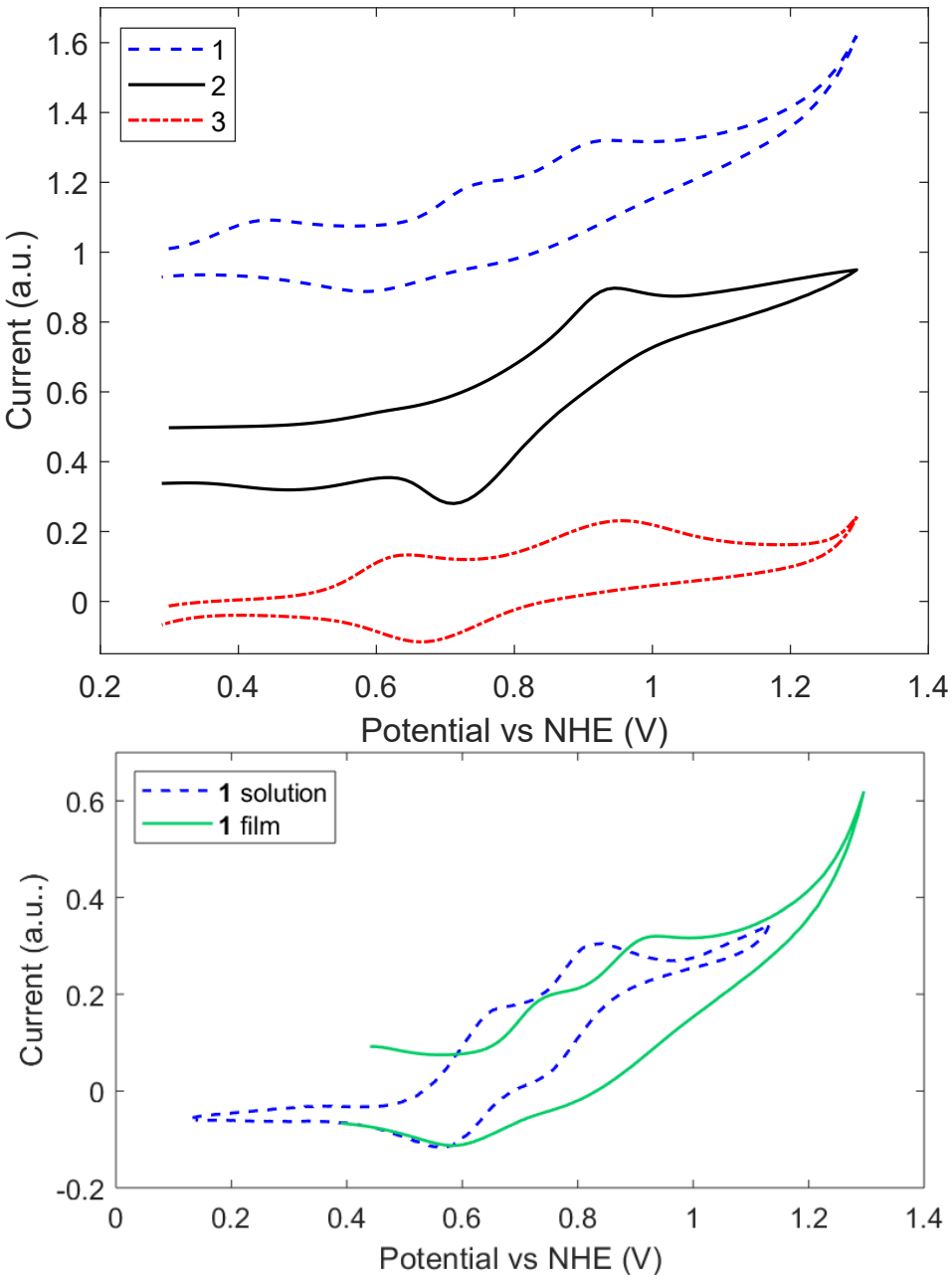

Figure S13: Cyclic voltammograms of coordination polymers **1**-**3**, deposited as thin films onto FTO (top); cyclic voltammogram of compound **1** as thin film overlayed with the voltammogram from solution (bottom). The redox potentials waves of the films (all vs NHE) were: **1** 0.66, 0.84; **2** (0.55), 0.83; **3** 0.81. The workfunctions of the lowest hole-accepting levels (in eV vs vac) are: **1** -5.28; **2** -5.27; **3** -5.25.

UV/Vis spectroscopy

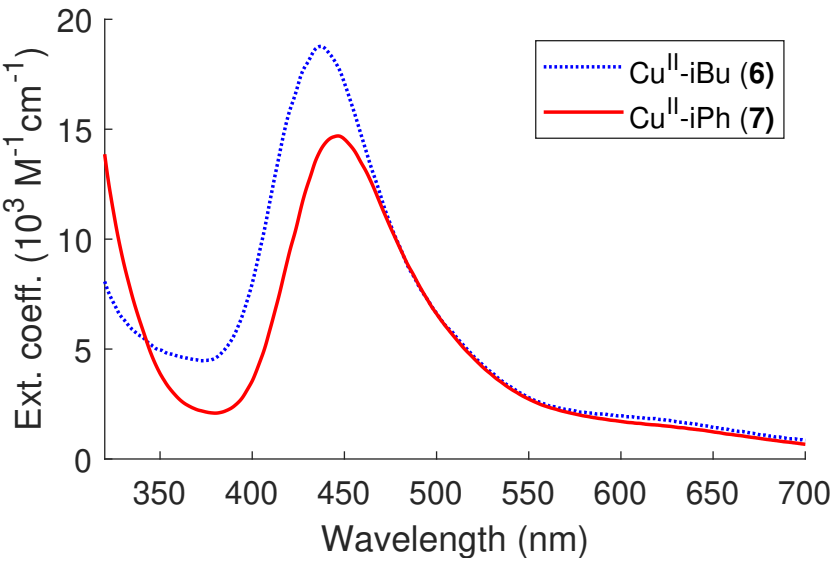

Figure S14: UV/Vis absorption spectra of Cu(II) units **6**-**7**.

Table S1: Electronic characterization of Cu(II) units **6**-**7**, from cyclic voltammetry and UV/Vis spectroscopy.

	E_0 vs NHE (V)	λ_{max} (nm)	$\epsilon_{\lambda max}$ ((M cm)$^{-1}$)
Cu^{II}-iBu (**6**)	0.63	436	18800
Cu^{II}-Ph (**7**)	0.67	447	14700

X-ray diffraction

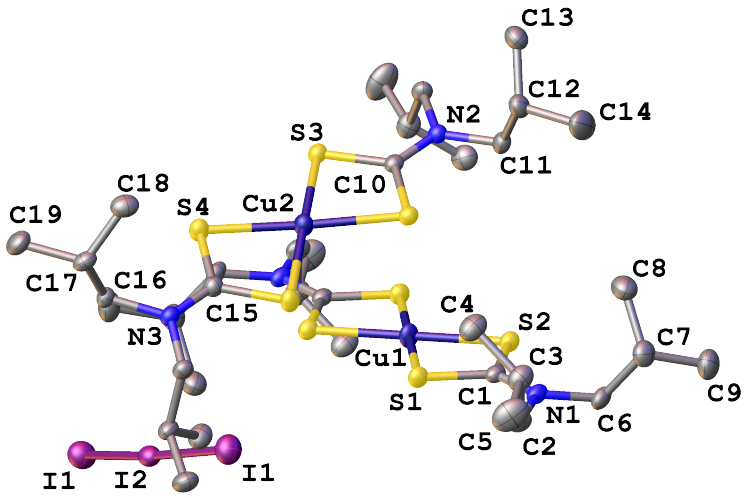

Figure S15: The sole identifiable crystal structure in polymers **2** comprises residual trihalide salts of copper dithiocarbamate dimers. This was, however, not matched by the bulk powder diffraction pattern (Fig. S18). The crystal structure with ellipsoids is drawn at the 50% probability level. For clarity hydrogen atoms and the atomic labels of symmetry equivalent atoms of the cations have been omitted.

Table S2: Crystal data and structure refinement.

Empirical formula	$C_{36}H_{72}Cu_2I_3N_4S_8$
Formula weight	1325.23
Temperature (K)	100.0(2)
Crystal system	monoclinic
Space group	C2/c
a (Å)	25.6269(3)
b (Å)	18.1627(3)
c (Å)	14.12980(15)
α (°)	90
β (°)	120.8970(9)
γ (°)	90
Volume (Å^3)	5423.25(13)
Z	4
ρ_{calc} (g cm^{-3})	1.623
μ (mm^{-1}) 2.700	
F(000)	1644.0
Crystal size (mm^3)	0.162 × 0.03 × 0.028
Radiation	Synchrotron (λ = 0.6889)
2θ range for data collection (°)	2.866 to 53.142
Index ranges	-31 $\leqslant$ h $\leqslant$ 31, -23 $\leqslant$ k $\leqslant$ 23, -18 $\leqslant$ l $\leqslant$ 18
Reflections collected	38858
Independent reflections	6219 [R_{int} = 0.0638, R_{sigma} = 0.0211]
Data/restraints/parameters	6217/0/252
Goodness-of-fit on F^2	1.063
Final R indexes [I $\geqslant 2\sigma$ (I)]	R_1 = 0.0297, wR_2 = 0.0775
Final R indexes [all data]	R_1 = 0.0330, wR_2 = 0.0794
Largest diff. peak/hole (e Å^{-3})	1.42/-1.05

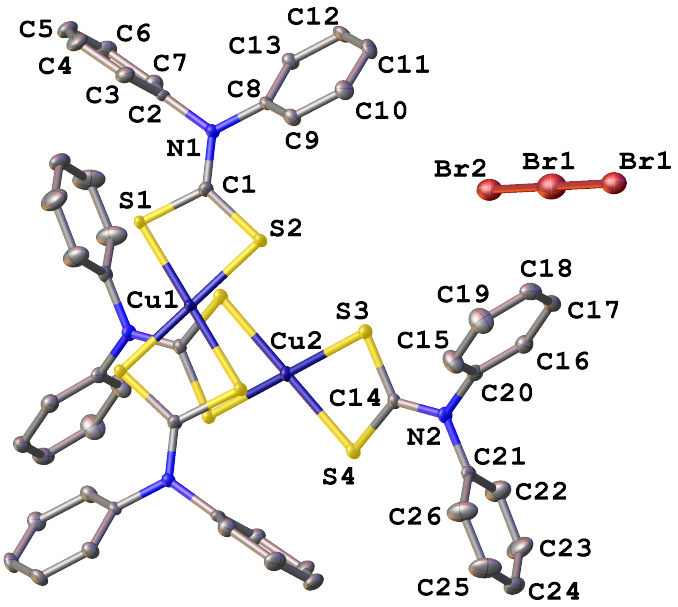

Figure S16: The sole identifiable crystal structure in polymers **3** comprises residual trihalide salts of copper dithiocarbamate dimers. This was, however, not matched by the bulk powder diffraction pattern (Fig. S18). The crystal structure with ellipsoids is drawn at the 50% probability level. For clarity hydrogen atoms and the atomic labels of symmetry equivalent atoms of the cations have been omitted.

Table S3: Crystal data and structure refinement.

Empirical formula	$C_{52}H_{40}Br_3Cu_2N_4S_8$
Formula weight	1344.17
Temperature (K)	100.0(2)
Crystal system	triclinic
Space group	P-1
a (Å)	7.97000(14)
b (Å)	12.38700(18)
c (Å)	14.1003(2)
α (°)	101.2360(13)
β (°)	99.4480(15)
γ (°)	96.4060(14)
Volume (Å^3)	1331.93(4)
Z	1
ρ_{calc} (g cm^{-3})	1.676
μ (mm^{-1}) 3.212	
F(000)	671.0
Crystal size (mm^3)	0.18 × 0.015 × 0.012
Radiation	Synchrotron (λ = 0.6889)
2θ range for data collection (°)	3.286 to 53.142
Index ranges	-10 $\leqslant$ h $\leqslant$ 10, -16 $\leqslant$ k $\leqslant$ 16, -18 $\leqslant$ l $\leqslant$ 18
Reflections collected	19132
Independent reflections	6039 [R_{int} = 0.0550, R_{sigma} = 0.0625]
Data/restraints/parameters	6039/0/316
Goodness-of-fit on F^2	1.137
Final R indexes [I $\geqslant 2\sigma$ (I)]	R_1 = 0.0409, wR_2 = 0.1249
Final R indexes [all data]	R_1 = 0.0454, wR_2 = 0.1278
Largest diff. peak/hole (e Å^{-3})	0.72/-1.93

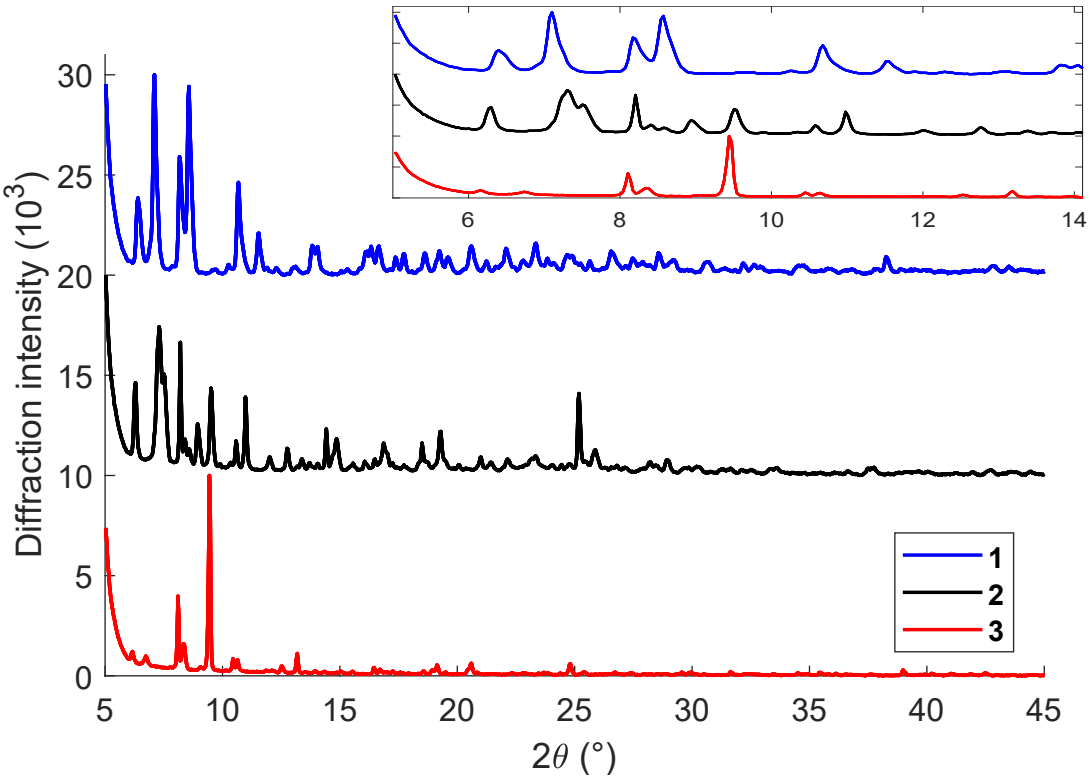

Figure S17: Powder X-ray diffractograms of coordination polymers **1**-**3**.

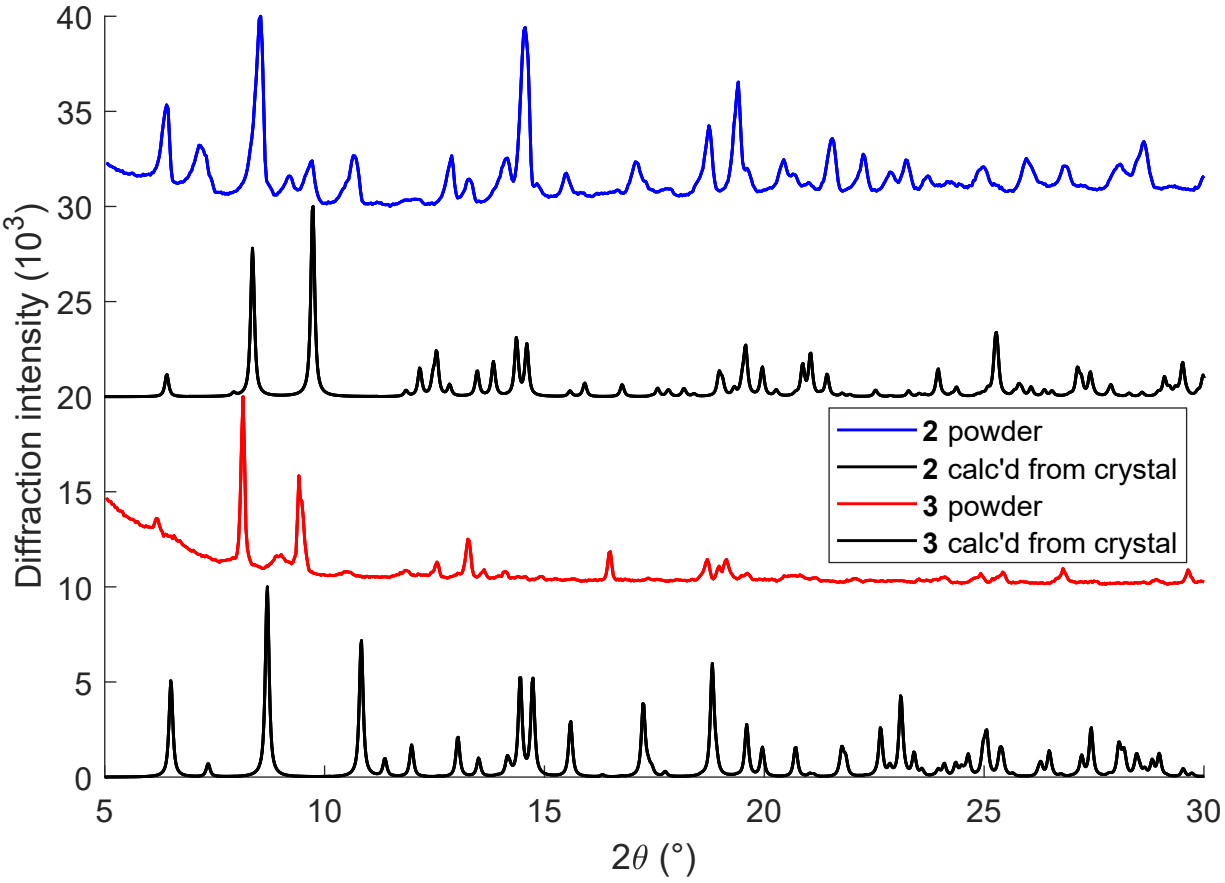

Figure S18: Powder X-ray diffractograms of coordination polymers **2** and **3** compared to the respective calculated pattern from the refined crystal structure. The sample of coordination polymer **1** had decomposed under the synchrotron beam during crystal analysis.

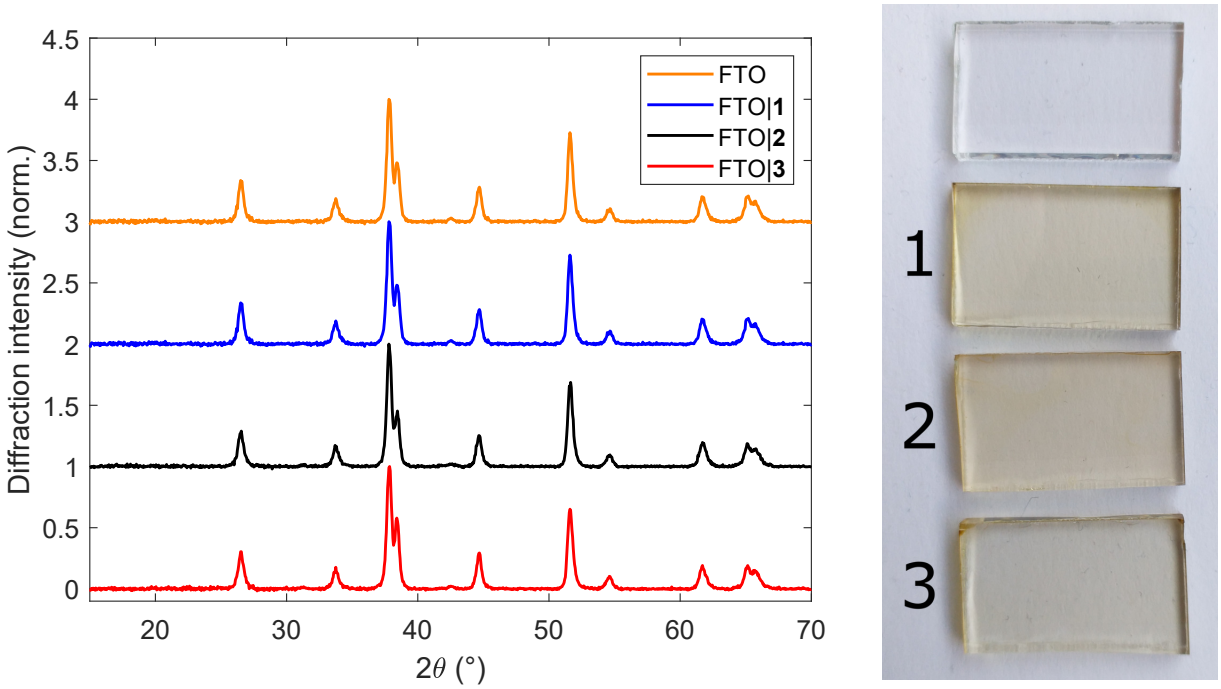

Figure S19: X-ray diffractograms of coordination polymer **1**-**3** thin films on F:SnO_2. A blank sample of F:SnO_2 glass was added for reference.

Raman spectroscopy

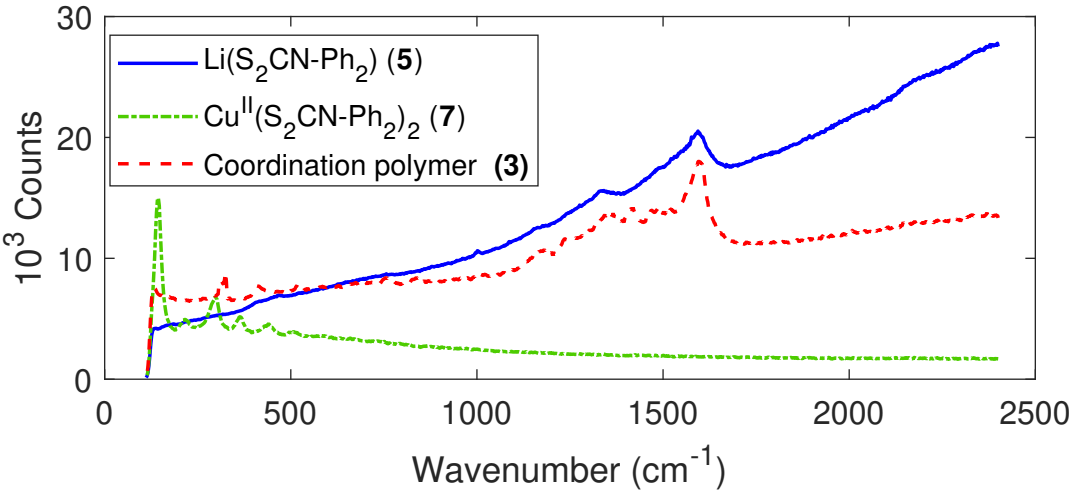

Figure S20: Raman spectra of ligand, Cu(II) unit and final coordination polymer for the diphenylamine-based compounds.

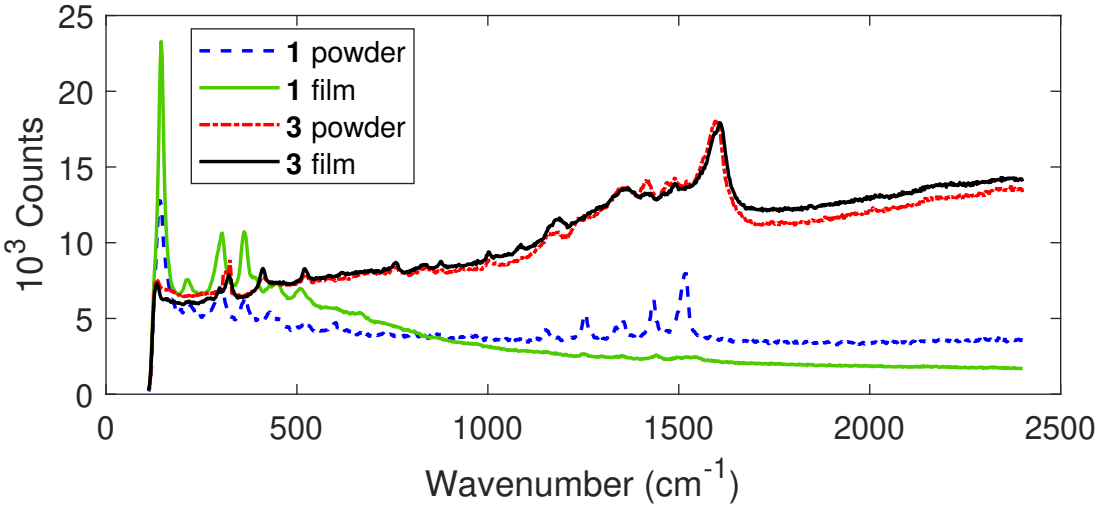

Figure S21: Raman spectra of powder and thin-film-deposited coordination polymers, for the examples of **1** and **3**.

Hole mobility

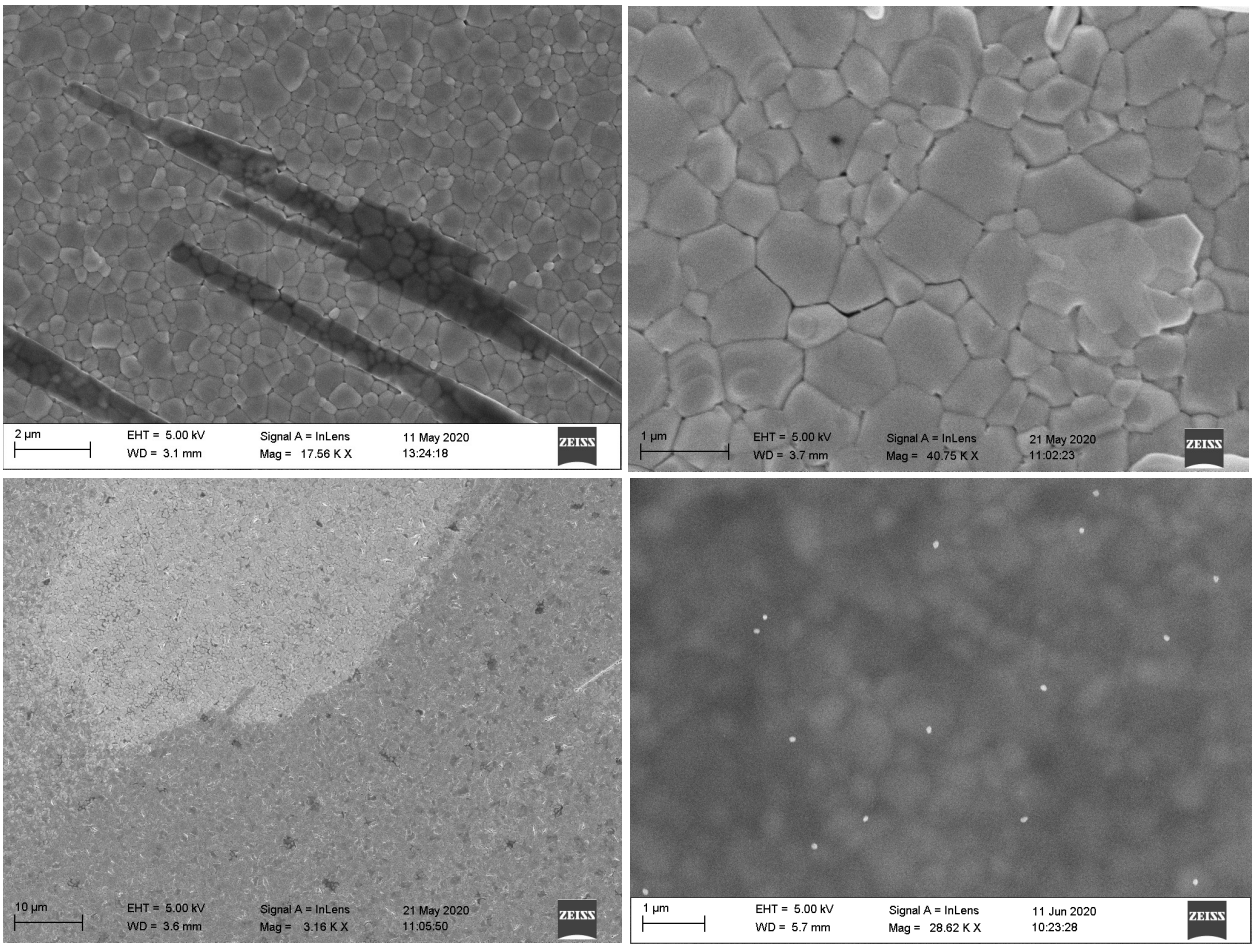

Figure S22: Electron microscopy images of thin film morphology, all films were for this example deposited onto a [CsFAMA]PbI_3 film. a) copper coordination polymer deposited onto perovskite without a pyridine base leads to crystal formation rather than a thin film. b) With the addition of a pyridine base, a homogeneous thin film of the polymer is obtained. The perovskite grains are indistinctly visible through the $\sim$100 nm copper coordination polymer film. c) same sample as in b, however showing one area where the polymer film was scratched during e.g. mounting. The bare perovskite (brighter) is visible, highlighting the contrast to the electron-poor hole-conducting copper polymer. d) perovskite grains appearing through a $\sim$150 nm layer of Spiro-MeOTAD.

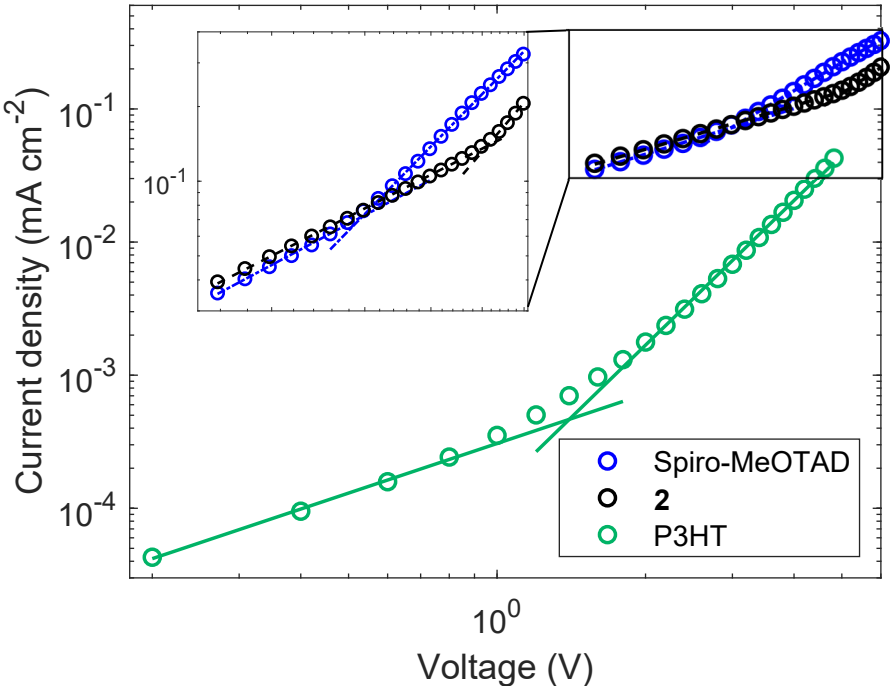

Figure S23: Space-charge limited current hole mobility measurements for reference materials Spiro-MeOTAD, poly(3-hexyl thiophene) (P3HT) and copper coordination polymer **2**. Extracted hole mobility for P3HT μ_h of 3.6 10^{-4} cm $(Vs)^{-1}$, compare Yang et al.: 3.8 10^{-4} cm $(Vs)^{-1}$.[S24]

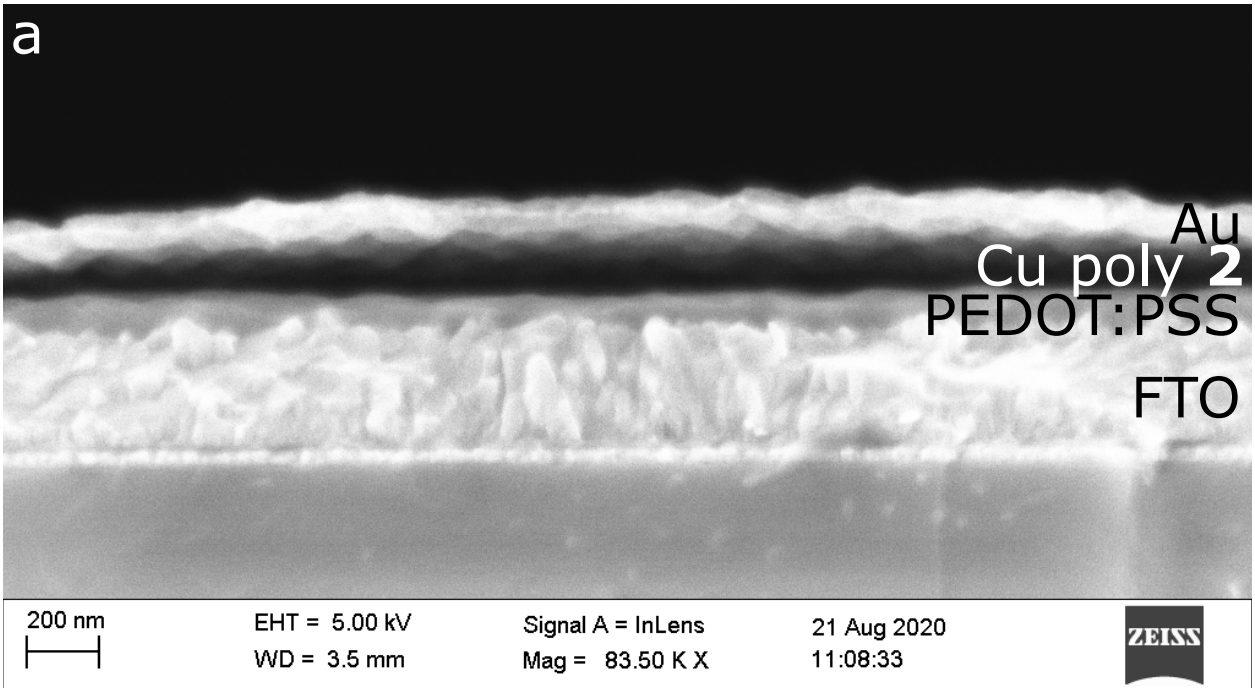

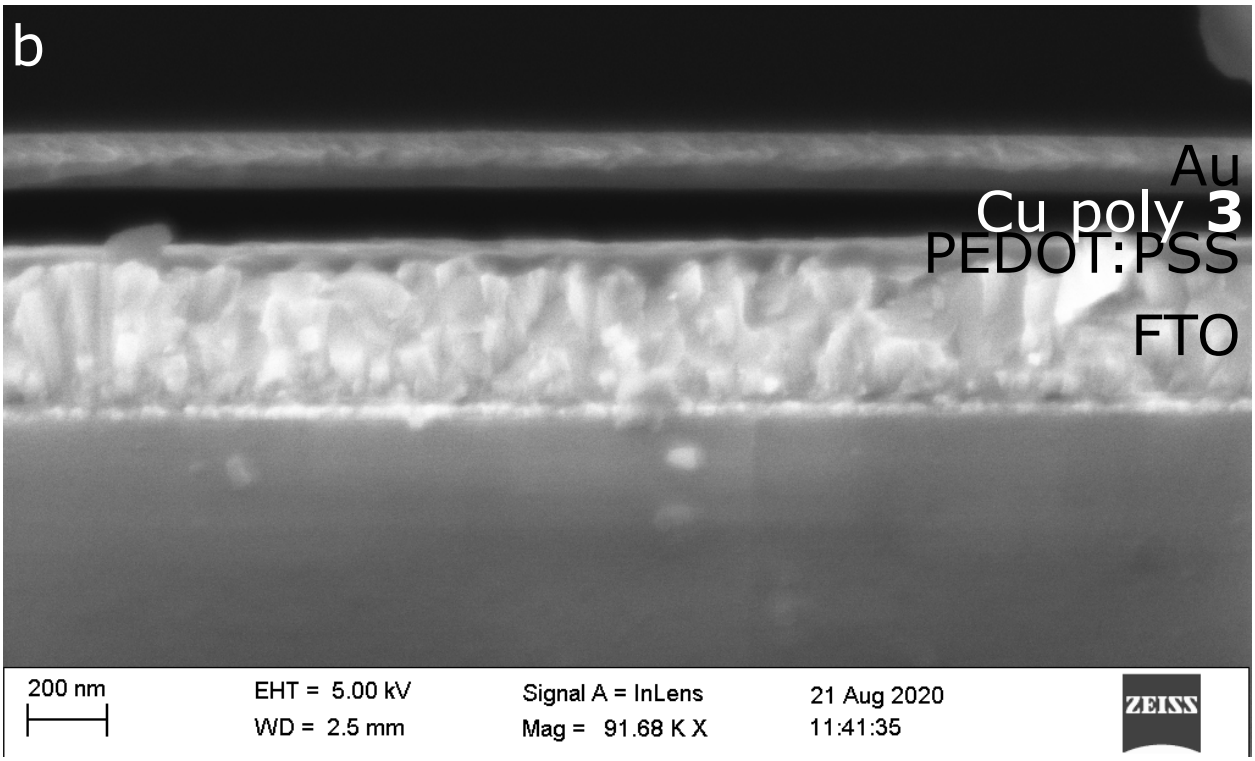

Figure S24: Crosssectional electron microscopy image of the 'hole-only' space-charge limited current sample for hole mobility measurements. a, FTO/PEDOT:PSS/**2**/Au; b, FTO/PEDOT:PSS/**3**/Au;.

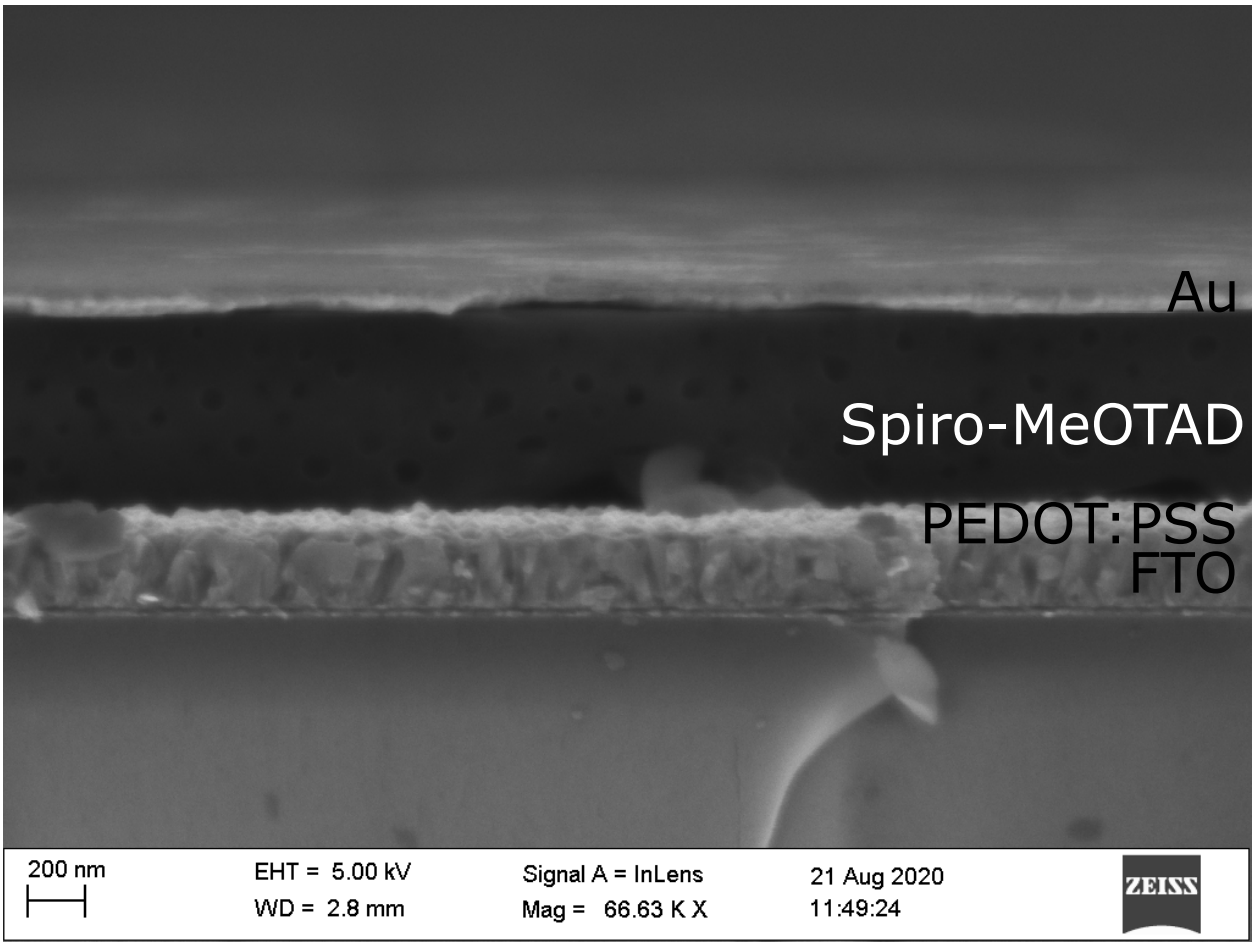

Figure S25: Crosssectional electron microscopy image of the 'hole-only' space-charge limited current sample for hole mobility measurements, here FTO/PEDOT:PSS/Spiro-MeOTAD/Au.

Conductivity

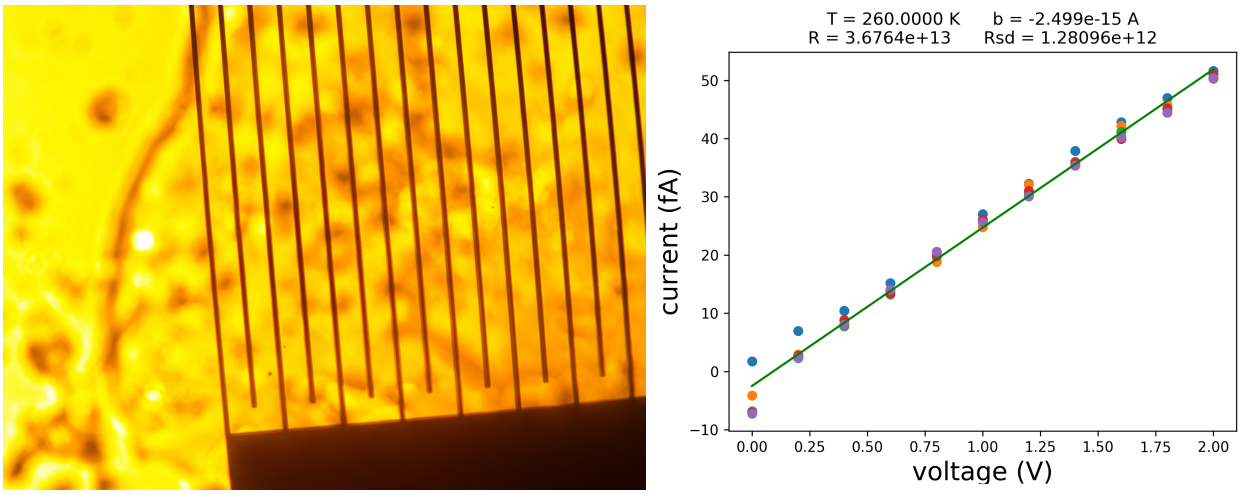

Figure S26: Left: Gold fingers deposited via photolithography for low-temperature conductivity measurements under the optical microscope; right: at low temperatures (here 260 K), the current-voltage sweeps on the gold contacts are still ohmic.

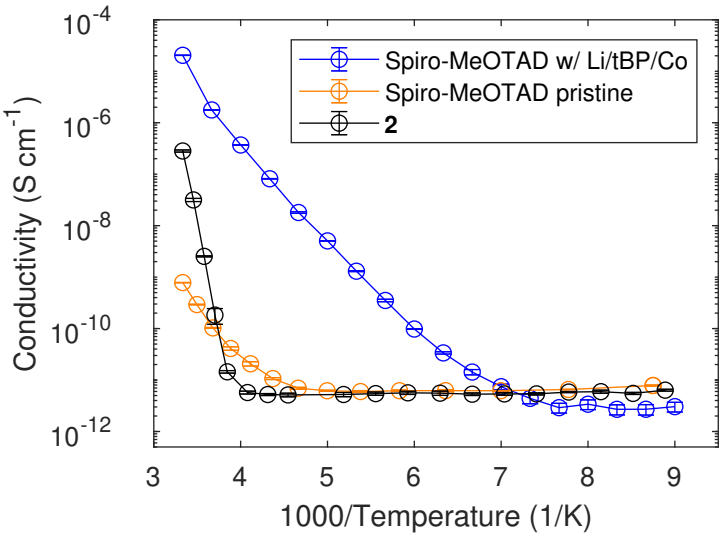

Figure S27: Temperature-dependent conductivity for reference material Spiro-MeOTAD (pristine as well as doped with LiTFSI, 4-*tert*-buty pyridine and cobalt FK209) and copper coordination polymer **2**.

Density Functional Theory Computations

Table S4: The structural models for the DFT calculations were created based on the crystal structures proposed in the work by Okubo et al.[S17], with the newly proposed side chains attached to the polymer backbone. After a relaxation of the full unit cell, single polymer chains were extracted as model systems for our calculations.

Compound	Chemical formula	a (Å)	b (Å)	c (Å)	α (°)	β (°)	γ (°)
1	$Br_4C_{44}Cu_6H_{84}N_8S_8$	10.3	12.7	20.8	79.8	111.5	90.1
2	$I_4C_{44}Cu_6H_{84}N_8S_8$	10.3	16.3	18.6	66.6	109.6	92.7

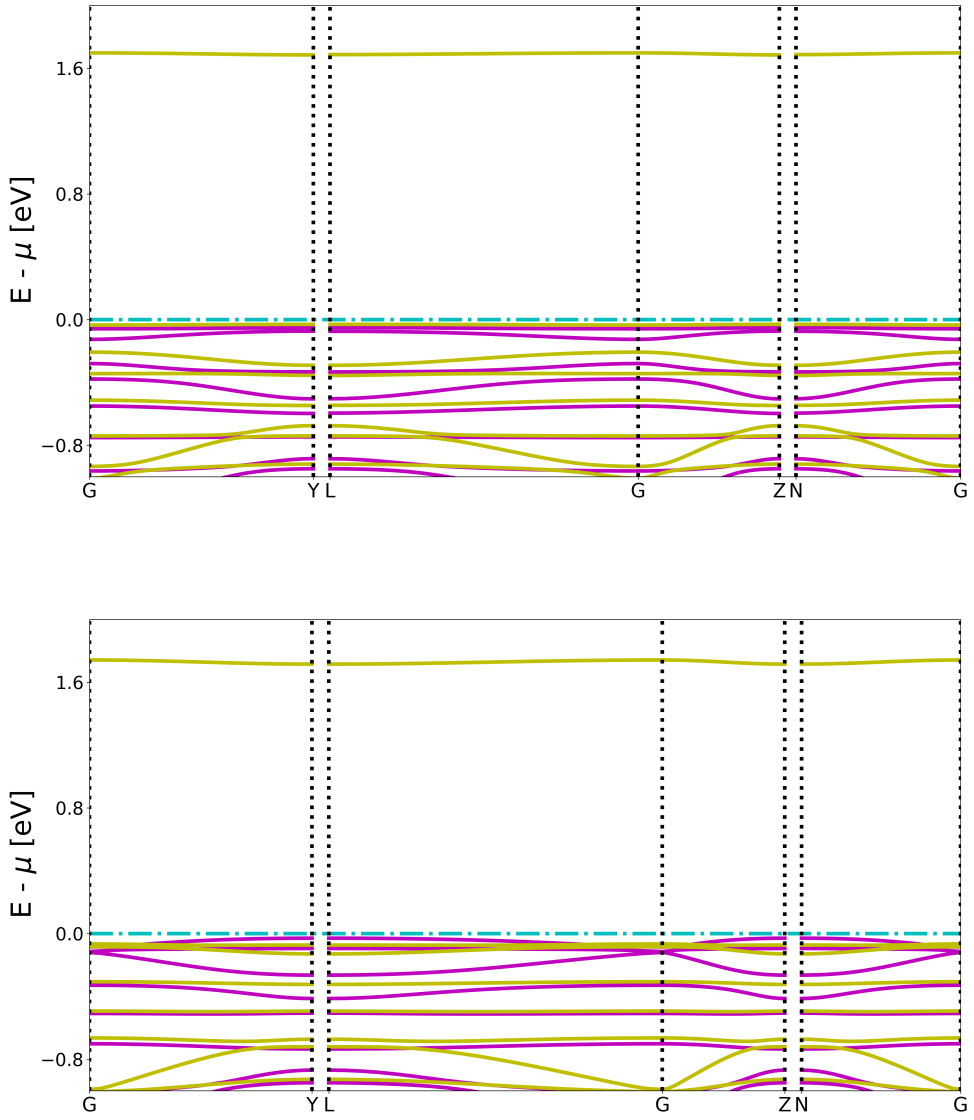

Figure S28: Band structures of the studied compounds **1** and **2** along high symmetry paths of the unit cell. Yellow and magenta distinguish the two spin channels.

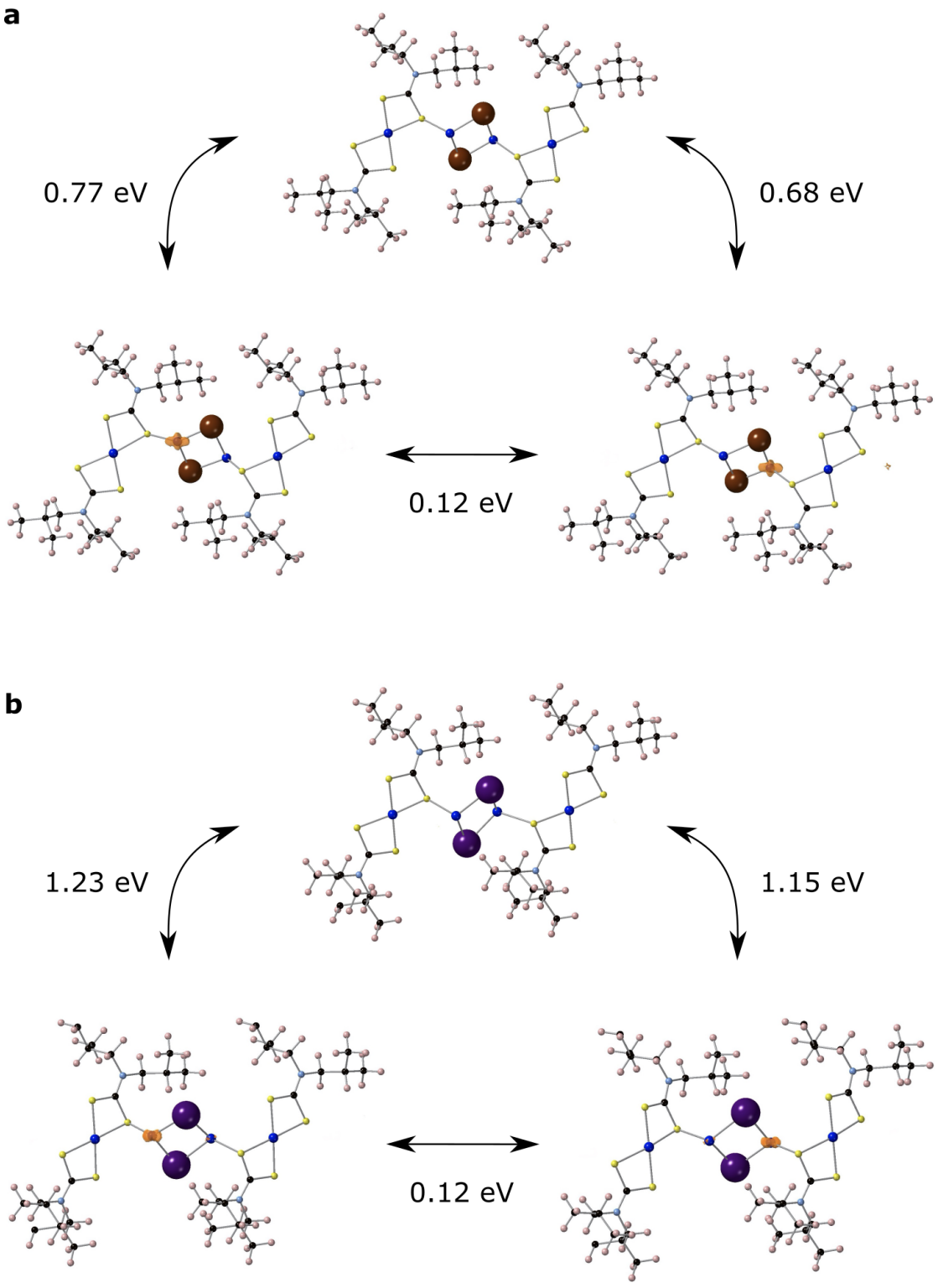

Figure S29: Calculated diabatic hole polaron spin densities and hoping barriers for discrete jumps between Cu sites of compounds **a, 1** and **b, 2** based on Marcus-Hush theory. On the copper dithiocarbamate units (top in each scheme), the hole polaron marks the absence of the d^9 electron and as such, no spin density is visible.

Photoluminescence

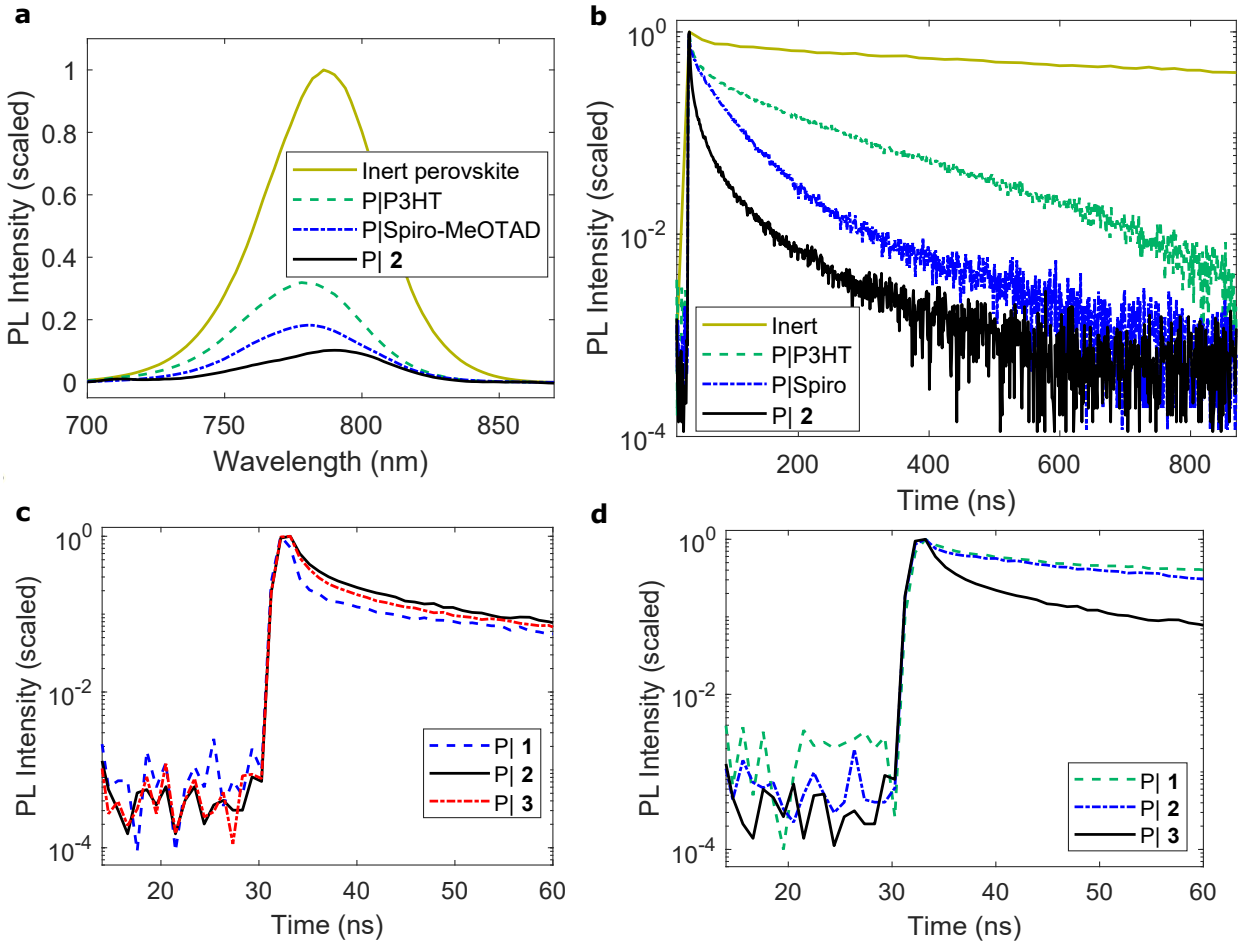

Figure S30: **a,** Steady-state and **b,** time-resolved photoluminescence of perovskite layers on microscope glass slides, and those with layers of hole transport materials poly(3-hexyl thiophene) (P3HT), Spiro-MeOTAD, and copper coordination polymer **2**. **c,** and **d,**, PL spectra and baselines at short timescales.

Table S5: Fit parameters for photoluminescence decay lifetimes.

	B1	τ_1 (ns)	Rel.1 (%)	B2	τ_2 (ns)	Rel.2 (%)	B3	τ_3 (ns)	Rel.3 (%)	τ_{Avg} (ns)
Perovskite inert	1543	279	3.4	3655	1267	36.5	1772	4298	60.1	3055
Pvsk|**1**	1031	15.4	22.2	308	181	77.8	-	-	-	144
Pvsk|**2**	8139	7.92	38.7	1570	64.9	61.3	-	-	-	43
Pvsk|**3**	8384	8.85	31.5	1265	127	68.5	-	-	-	90
Pvsk|P3HT	3951	27.9	11.5	3991	212	88.5	-	-	-	191
Pvsk|Spiro-MeOTAD	5131	35.2	63.1	803	131	36.9	-	-	-	71

Solar cell characterization

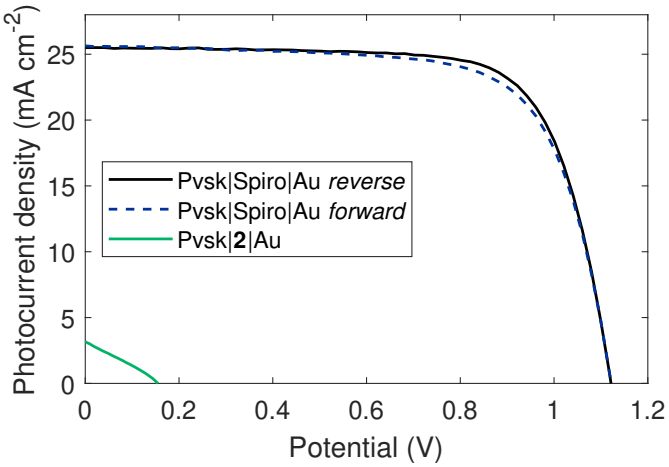

Figure S31: Solar-cell characterization for gold counter electrode devices, using copper coordination polymer **2** and Spiro-MeOTAD as hole transport materials.

Table S6: Photovoltaic parameters for gold counter electrode devices, using copper coordination polymer **2** and Spiro-MeOTAD as hole transport materials.

		V_{OC} (V)	J_{SC} (mA cm^{-2})	FF	PCE (%)	Hysteresis index
Pvsk|Spiro|Au	reverse	1.12 1.09±0.02	25.5 25.5±0.34	0.730 0.745±0.01	20.9 20.6±0.71	0.01 0.05±0.05
	forward	1.12 1.08±0.02	25.6 25.4±0.30	0.705 0.689±0.03	20.3 18.9±0.96	
Pvsk|**2**| Au		0.155	3.17	0.282	0.14	

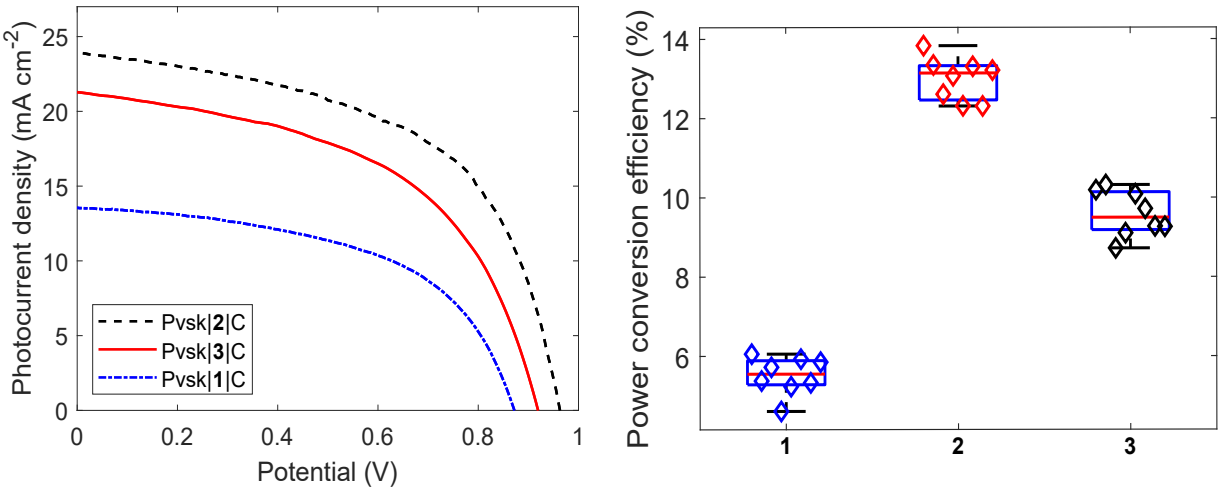

Figure S32: Characterization of solar cells using the copper coordination polymers **1**-**3** as hole transport materials. Champion cells presented as J-V curves and statistics.

Table S7: Photovoltaic parameters for solar cells using the copper coordination polymers **1**-**3** as hole transport materials.

	V_{OC} (V)	J_{SC} (mA cm^{-2})	FF	PCE (%)
Pvsk|**1**|C	0.842 0.820±0.02	13.6 13.1±0.48	0.537 0.513±0.03	6.05 5.51±0.47
Pvsk|**2**|C	0.970 0.956±0.01	23.0 23.0±0.58	0.620 0.591±0.02	13.8 13.0±0.54
Pvsk|**3**|C	0.918 0.906±0.02	21.3 21.2±0.62	0.516 0.499±0.02	10.2 9.59±0.58

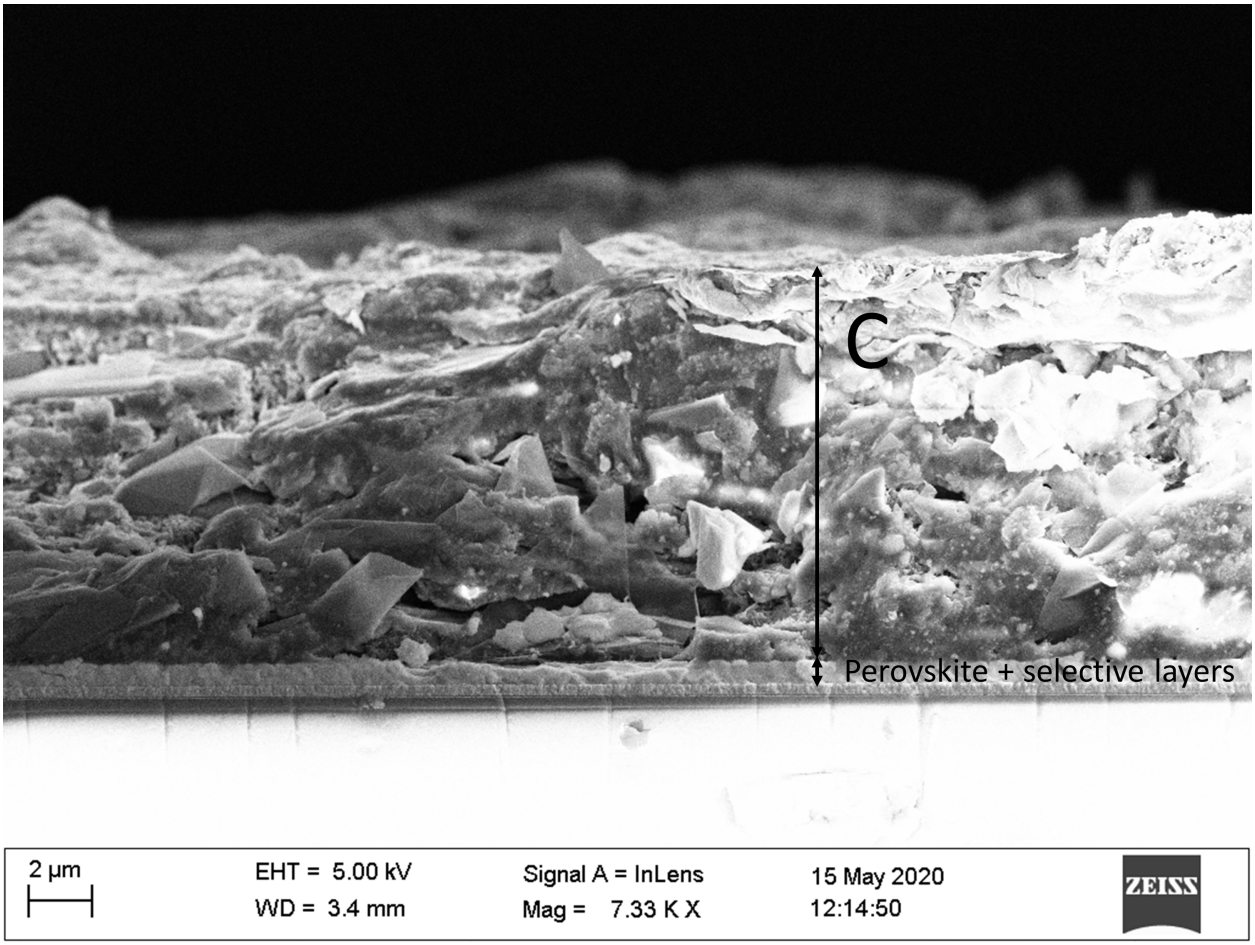

Figure S33: Crosssectional electron microscopy image of a solar cell with copper coordination polymer **2** as hole transport material (FTO/SnO_2/Pvsk/**2**/C).

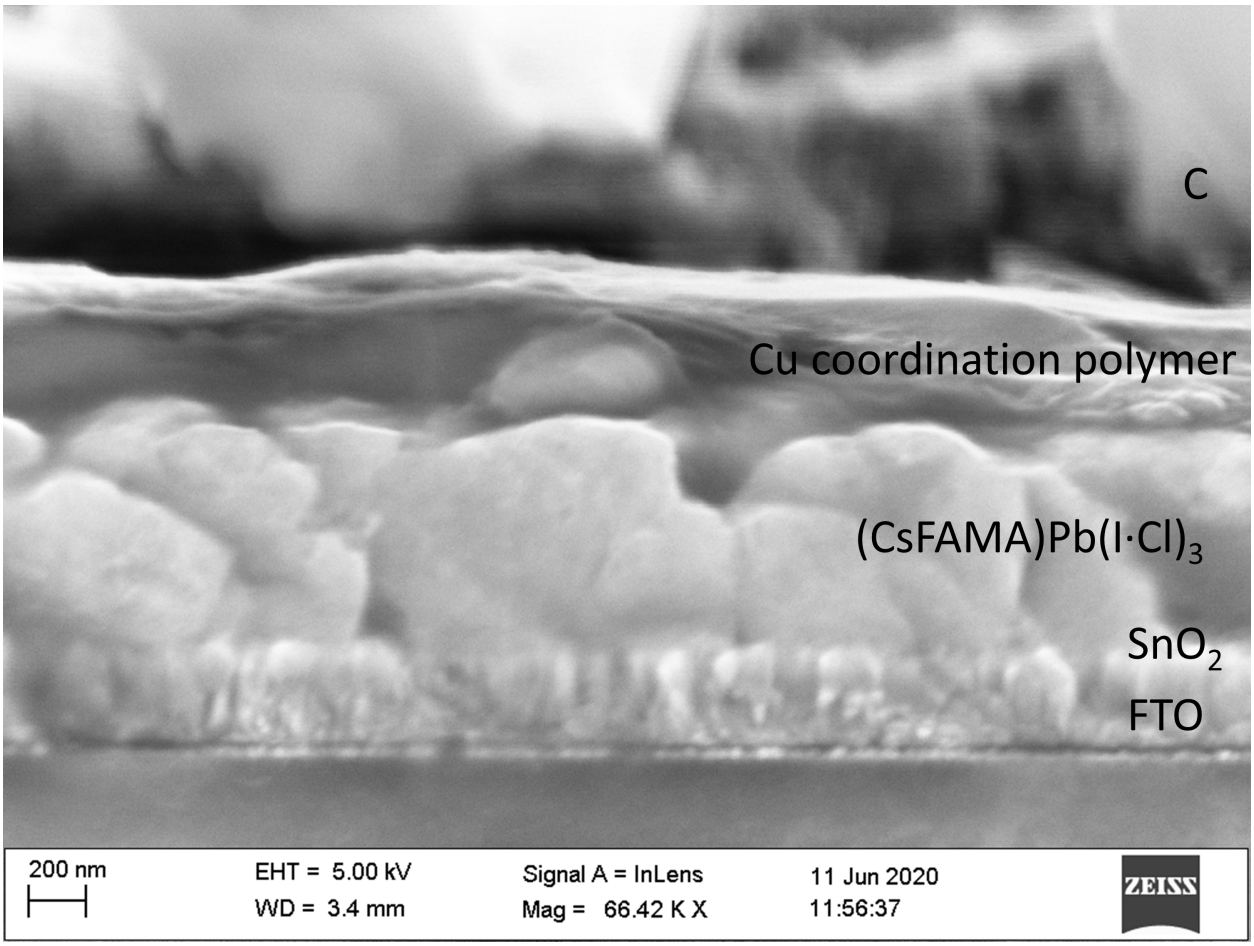

Figure S34: Crosssectional electron microscopy image of a solar cell with copper coordination polymer **2** as hole transport material (FTO/SnO_2/Pvsk/**2**/C), focusing on the layers underneath the carbon electrode.

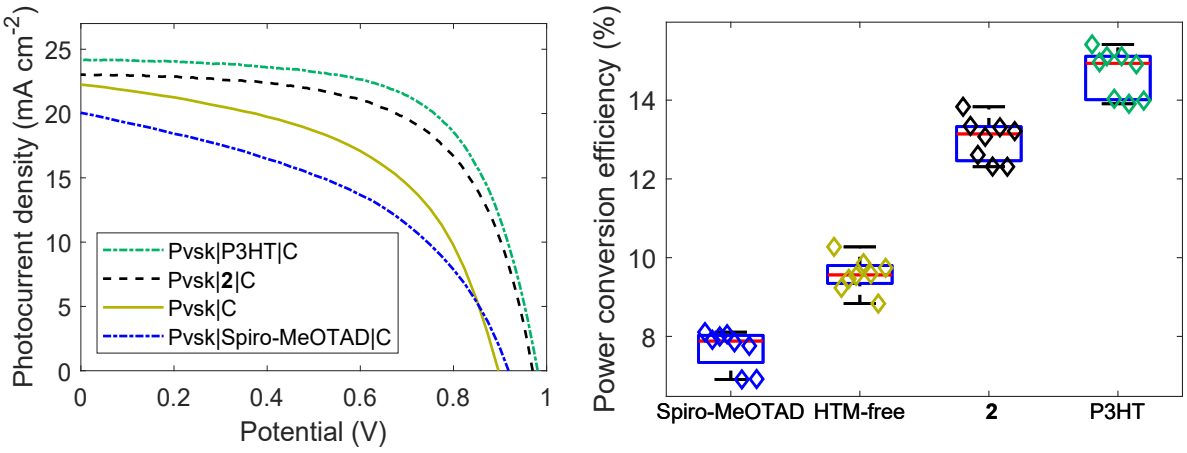

Figure S35: Characterization of solar cells using poly(3-hexyl thiophene) (P3HT), Spiro-MeOTAD and copper coordination polymer **2** as hole transport materials. Devices without any *p*-selective layer were added for reference. Champion cells presented as J-V curves and statistics.

Table S8: Photovoltaic parameters for solar cells using poly(3-hexyl thiophene) (P3HT), Spiro-MeOTAD and copper coordination polymer **2** as hole transport materials. Devices without any *p*-selective layer were added for reference.

	V_{OC} (V)	J_{SC} (mA cm^{-2})	FF	PCE (%)
Pvsk|P3HT|C	0.981 0.966±0.01	24.2 23.9±0.51	0.650 0.635±0.02	15.4 14.7±0.60
Pvsk|**2**|C	0.970 0.956±0.01	23.0 23.0±0.58	0.620 0.591±0.02	13.8 13.0±0.54
Pvsk|C	0.894 0.875±0.01	22.2 21.8±0.55	0.525 0.501±0.02	10.3 9.57±0.43
Pvsk|Spiro-MeOTAD|C	0.913 0.889±0.03	19.8 19.3±68	0.451 0.449±0.02	8.11 7.69±0.49

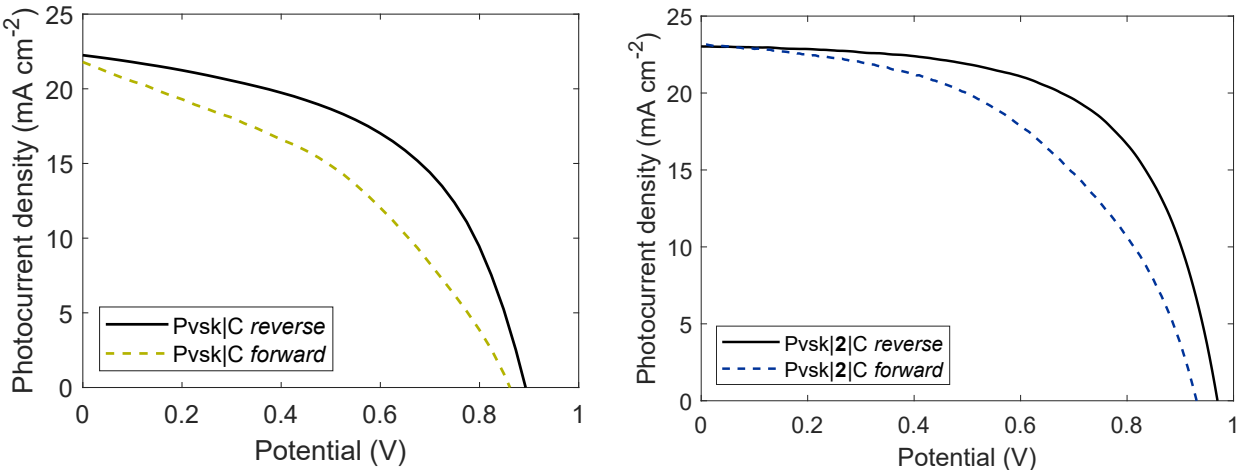

Figure S36: Forward and backward scans of solar cells without a hole transport material layer, as well as those with copper coordination polymer **2**.

Table S9: Photovoltaic parameters for forward and backward scans of solar cells without a hole transport material layer, as well as those with copper coordination polymer **2**.

		V_{OC} (V)	J_{SC} mA cm^{-2}	FF	PCE (%)	Hysteresis index balance-adjusted	Hysteresis index conventional
Pvsk|C	forward	0.862	21.8	0.398	7.14	0.184	0.307
	reverse	0.894	22.2	0.526	10.3		
Pvsk|**2**|C	forward	0.931	23.0	0.499	10.7	0.126	0.225
	reverse	0.970	23.0	0.620	13.8		

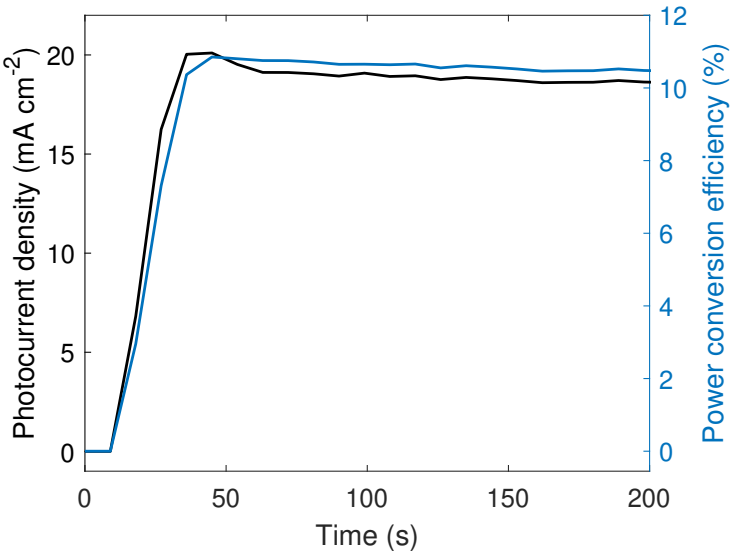

Figure S37: Stabilized photocurrent and power output of a solar cell employing copper coordination polymer **2** as hole transport material. V_{mpp} = 0.565 V, J_{mpp} = 18.6 mA cm^{-2}, P_{mpp} = 10.5 mW cm^{-2}, η = 10.5%.

Supporting references

[S1] Kellner, R. & St. Nikolov, G. Far ir spectra of dithiocarbamate complexes correlations with structure parameters. *Journal of Inorganic and Nuclear Chemistry* **43**, 1183–1188 (1981).

[S2] Tiwari, S., Reddy, K., Bajpai, A., Khare, K. & Nagaraju, V. Synthesis and characterization of bisdithiocarbamates from weak nitrogen bases and its metal complexes. *International Research Journal of Pure and Applied Chemistry* **7**, 78–91 (2015).

[S3] Ajibade, P. A., Mbese, J. Z. & Omondi, B. Group 12 dithiocarbamate complexes: Synthesis, characterization, and x-ray crystal structures of zn(ii) and hg(ii) complexes and their use as precursors for metal sulfide nanoparticles. *Inorganic and Nano-Metal Chemistry* **47**, 202–212 (2017).

[S4] Johnson, N. T., Waddell, P. G., Clegg, W. & Probert, M. R. Remote Access Revolution: Chemical Crystallographers Enter a New Era at Diamond Light Source Beamline I19. *Crystals* **7**, 360 (2017).

[S5] Allan, D. R. *et al.* A Novel Dual Air-Bearing Fixed-χ Diffractometer for Small-Molecule Single-Crystal X-ray Diffraction on Beamline I19 at Diamond Light Source. *Crystals* **7**, 336 (2017).

[S6] Sheldrick, G. M. SHELXT – Integrated space-group and crystal-structure determination. *Acta Cryst A* **71**, 3–8 (2015).

[S7] Sheldrick, G. M. A short history of SHELX. *Acta Cryst A* **64**, 112–122 (2008).

[S8] Dolomanov, O. V., Bourhis, L. J., Gildea, R. J., Howard, J. a. K. & Puschmann, H. OLEX2: A complete structure solution, refinement and analysis program. *J Appl Cryst* **42**, 339–341 (2009).

[S9] Snaith, H. J. & Grätzel, M. Enhanced charge mobility in a molecular hole transporter via addition of redox inactive ionic dopant: Implication to dye-sensitized solar cells. *Applied Physics Letters* **89**, 262114 (2006).

[S10] Blum, V. *et al.* Ab initio molecular simulations with numeric atom-centered orbitals. *Computer Physics Communications* **180**, 2175–2196 (2009).

[S11] Havu, V., Blum, V., Havu, P. & Scheffler, M. Efficient integration for all-electron electronic structure calculation using numeric basis functions. *Journal of Computational Physics* **228**, 8367–8379 (2009).

[S12] Levchenko, S. V. *et al.* Hybrid functionals for large periodic systems in an all-electron, numeric atom-centered basis framework. *Computer Physics Communications* **192**, 60–69 (2015).

[S13] Marek, A. *et al.* The ELPA library: scalable parallel eigenvalue solutions for electronic structure theory and computational science. *Journal of Physics: Condensed Matter* **26**, 213201 (2014).

[S14] Ren, X. *et al.* Resolution-of-identity approach to Hartree–Fock, hybrid density functionals, RPA, MP2 and *GW* with numeric atom-centered orbital basis functions. *New Journal of Physics* **14**, 053020 (2012).

[S15] Nemnes, G. A. *et al.* How measurement protocols influence the dynamic j-v characteristics of perovskite solar cells: Theory and experiment. *Solar Energy* **173**, 976–983 (2018).

[S16] NREL. Reference Air Mass 1.5 Spectra. https://www.nrel.gov/grid/solar-resource/spectra-am1.5.html. Accessed: 2018-03-28.

[S17] Okubo, T. *et al.* Magnetic and conducting properties of new halide-bridged mixed-valence cui-cuii 1d coordination polymers including a hexamethylene dithiocarbamate ligand. *Inorganic Chemistry* **49**, 3700–3702 (2010).

[S18] Ngo, S. C., Banger, K. K., DelaRosa, M. J., Toscano, P. J. & Welch, J. T. Thermal and structural characterization of a series of homoleptic cu(ii) dialkyldithiocarbamate complexes: bigger is only marginally better for potential mocvd performance. *Polyhedron* **22**, 1575–1583 (2003).

[S19] Padungros, P. & Wei, A. Practical synthesis of aromatic dithiocarbamates. *Synthetic Communications* **44**, 2336–2343 (2014).

[S20] Kim, Y. J. *et al.* Effect of layer-by-layer assembled sno2 interfacial layers in photovoltaic properties of dye-sensitized solar cells. *Langmuir* **28**, 10620–10626 (2012).

[S21] Han, G. S. *et al.* Spin-coating process for 10 cm × 10 cm perovskite solar modules enabled by self-assembly of sno2 nanocolloids. *ACS Energy Letters* **4**, 1845–1851 (2019).

[S22] Arora, N. *et al.* Perovskite solar cells with cuscn hole extraction layers yield stabilized efficiencies greater than 20%. *Science* **358**, 768–771 (2017).

[S23] Zhao, P. *et al.* Antisolvent with an ultrawide processing window for the one-step fabrication of efficient and large-area perovskite solar cells. *Advanced Materials* **30**, 1802763 (2018).

[S24] Yang, K., Wang, Y., Jain, A., Samulson, L. & Kumar, J. Determination of electron and hole mobility of regioregular poly(3-hexylthiophene) by the time of flight method. *Journal of Macromolecular Science, Part A* **44**, 1261–1264 (2007).